

**Force Feedback for the Patient Side Manipulator  
of the daVinci Research Kit**

by

Anna Novoseltseva

A Thesis submitted to the Faculty of the

WORCESTER POLYTECHNIC INSTITUTE

in partial fulfillment of the requirements for the

Degree of Master of Science in Biomedical Engineering

Worcester, Massachusetts

May, 2018

© Anna Novoseltseva 2018

All rights reserved

Approved by:

---

Prof. Gregory S. Fischer, Advisor  
Worcester Polytechnic Institute

---

Prof. Karen Troy, Committee Member  
Worcester Polytechnic Institute

---

Prof. Loris Fichera, Committee Member  
Worcester Polytechnic Institute

# Abstract

Teleoperated robotic surgical systems such as daVinci are widely used for laparoscopic surgeries. The currently available daVinci system does not provide haptic feedback. Prior research has shown that the addition of haptic feedback improves surgeons' performance during minimally invasive surgeries. Other authors have implemented haptic feedback in the daVinci robot by placing sensors on the surgical tools, using visual force estimation, and measuring proximal guide wire forces. However, issues with biocompatibility, time delay, low accuracy, and repeatability make them impractical for clinical use. In this work, two strain gauge force-sensing devices were created for the patient side manipulator of the daVinci surgical robot. These devices were designed to be easily added to the existing system. The device mounted on the cannula measures the X-Y components of the forces applied to the tool, and the device mounted on the sterile adapter measures the Z-component of the force. These devices are used for the real-time force feedback in the daVinci robot. The proposed system has high sensitivity and resolution, matches the required force measurement range, and has high signal-to-noise ratio, which implies high signal quality. However,

the absolute errors of the currently built devices are high due to the manufacturing techniques used on the prototype that could be improved upon for a deployed device. This work demonstrates fast 3-DOF force measurements on the daVinci robot without any robot or instrument modifications. While the present system has significant systematic errors, these can be mitigated by altering the mechanical design to reduce hysteresis and improve the accuracy of the system.

# Acknowledgments

I would first like to thank my thesis advisor Professor Gregory Fischer. Prof. Fischer always guided me throughout my research by giving me valuable and timely advisement.

I would also like to thank the experts who were involved in the validation of this research project: Prof. Karen Troy and Prof. Loris Fichera. Without their participation and input, the validation could not have been successfully conducted.

I would also like to thank my lab mates Adnan Munawar, Radian Azhar Gondokaryono, Paulo Carvalho, Joseph Schornak, Abhishek Kashyap, Chris Nycz for giving me with valuable pieces of advice.

Finally, I must express my profound gratitude to my parents and to my boyfriend for providing me with unfailing support and continuous encouragement throughout my years of study and through the process of researching and writing this thesis. This accomplishment would not have been possible without them. Thank you.

# Contents

<b>Abstract</b>	iii
<b>Acknowledgments</b>	v
<b>List of Tables</b>	vii
<b>List of Figures</b>	viii
<b>1 Introduction</b>	1
<b>2 Background</b>	3
2.1 Teleoperated Surgical Robots . . . . .	3
2.2 Importance of Haptic Feedback . . . . .	7
2.3 Current Approaches . . . . .	13
2.3.1 Sensor Placement on Instrument . . . . .	13
2.3.2 New Instrument Designs . . . . .	14
2.3.3 Sensorless Methods . . . . .	15
2.4 Force Sensing Technologies . . . . .	17

2.5 Contributions . . . . .	19
<b>3 Force Sensor Design and Characterization</b>	<b>20</b>
3.1 Requirements for the System . . . . .	20
3.2 Force Measurement . . . . .	23
3.3 Mechanical Design . . . . .	24
3.3.1 X-Y Device . . . . .	24
3.3.2 Z Device . . . . .	25
3.4 Sensor Selection and Placement Optimization . . . . .	27
3.4.1 Sensor Placement Optimization . . . . .	28
3.4.1.1 Elastic Modulus Measurements . . . . .	28
3.4.1.2 Density Measurements . . . . .	30
3.4.1.3 Simulation Results . . . . .	30
3.4.2 Strain Gauge . . . . .	32
3.4.3 Installation of Strain Gauges . . . . .	33
3.5 Electrical and Software Design . . . . .	35
3.5.1 Circuit design . . . . .	35
3.5.2 Noise Analysis . . . . .	38
3.5.3 Microcontroller Software . . . . .	39
3.5.4 ROS Architecture . . . . .	40
3.6 Calibration . . . . .	41
3.6.1 Calibration System . . . . .	41

3.6.2	Calibration of the Load Cell . . . . .	45
3.7	Results . . . . .	46
3.7.1	Calibration Results . . . . .	46
3.7.2	Calibration Curve Dependence from Sterile Adapter Position .	52
<b>4</b>	<b>Discussion and Conclusion</b>	<b>55</b>
4.1	Mechanical Design Issues . . . . .	56
4.2	Electrical Design Issues . . . . .	59
4.3	Conclusion . . . . .	60
<b>References</b>		<b>61</b>

# List of Tables

3.1	Elasticity Modulus Measurement Data . . . . .	30
3.2	Material Properties . . . . .	32
3.3	Sensors Characteristics . . . . .	51

# List of Figures

2.1	The daVinci Si Surgical System . . . . .	5
2.2	The Senhance Surgical System . . . . .	6
2.3	Effects of Visual Force Feedback on Robot-Assisted Surgical Task Performance . . . . .	8
2.4	Examination of Blunt Dissection with/without Force Feedback . . . . .	10
2.5	Bimanual Peg Board Experiment Results . . . . .	12
2.6	Prototype of the 2-DOF Compliant Forceps . . . . .	14
2.7	Optical Force Sensor . . . . .	15
2.8	Force-Sensing Surgical Tool . . . . .	16
2.9	Flowchart of Vision-Based Force Estimation Approach . . . . .	16
3.1	Cannula Placement Inside a Patient on the daVinci Si System . . . . .	21
3.2	Developed Force Measuring System Attached to the PSM . . . . .	23
3.3	Block Diagram . . . . .	24
3.4	XY-direction Force Feedback Sensor . . . . .	24
3.5	Displacement of the XY Device . . . . .	25
3.6	Z-direction Force Feedback Sensor . . . . .	26
3.7	Z-direction Force Feedback Sensor (Section View) . . . . .	27
3.8	Setup to Measure Elastic Modulus . . . . .	29
3.9	Strain in the Device to Measure Forces in X-Y Direction . . . . .	31
3.10	Strain in the Device to Measure Forces in Z Direction . . . . .	31
3.11	Materials for Strain Gauge Application . . . . .	34
3.12	Block Diagram of the Circuit . . . . .	35
3.13	Wheatstone Bridge Configuration of the XY-device . . . . .	36
3.14	Wheatstone Bridge Configuration of the Z-device . . . . .	36
3.15	Manufactured PCB . . . . .	37
3.16	FFT Analysis Results . . . . .	38
3.17	ADC LTC1865 Operating Sequence . . . . .	39
3.18	ROS Architecture . . . . .	40
3.19	Photo of the Calibration Setup . . . . .	42
3.20	Block Diagram of the Calibration Setup . . . . .	43
3.21	Block Diagram of the Load Cell Calibration Setup . . . . .	45

3.22 Load Cell Calibration Result . . . . .	46
3.23 Calibration Results of XY Device . . . . .	47
3.24 Calibration Results in Z-direction . . . . .	48
3.25 Sterile Adapter Movement . . . . .	52
3.26 Sterile Adapter Position Calibration Results for X-direction . . . . .	53
3.27 Sterile Adapter Position Calibration Results for Y-direction . . . . .	54
4.1 Actual and Measured Forces in X-direction . . . . .	56
4.2 Lower Face of the X-Y Device without Tool Shaft . . . . .	57
4.3 New X-Y Device Design . . . . .	58
4.4 1st Instrumentation Amplifier . . . . .	68
4.5 2nd Instrumentation Amplifier . . . . .	69
4.6 USB-UART Interface . . . . .	70
4.7 Microcontroller and Power Source . . . . .	71
4.8 Voltage Converter . . . . .	72
4.9 PCB Layout . . . . .	73
4.10 PCB Materials Bill (1) . . . . .	75
4.11 PCB Materials Bill (2) . . . . .	76
4.12 Mechanical and Strain Gauge Materials Bill . . . . .	77

Disclaimer: certain materials are included under the fair use exemption of the U.S. Copyright Law and have been prepared according to the fair use guidelines and are restricted from further use.

# Acronyms

**PSM** Patient Side Manipulator

**DOF** Degrees of Freedom

**CAD/CAM** Computer-Aided Design/Computer-Aided Manufacturing

**QTC Pills** Quantum Tunneling Composite Pills

**RMS** Root Mean Square

**PCB** Printed Circuit Board

**ROS** Robot Operating System

**SD** Standard Deviation

**SNR** Signal-to-noise Ratio

**GF** Gauge Factor

**ADC** Analog to Digital Converter

**FFT** Fast Fourier transform

**RMSE** Root Mean Square Error

# Chapter 1

## Introduction

The daVinci surgical system is a robotic platform that enhances surgeons performance in minimally invasive surgeries by enabling highly precise translation of surgeon's hand movements to the instrument's movements.

The currently available daVinci surgery system has a laparoscopic camera, providing visual feedback to guide doctors during surgery. However, the system does not have any kinesthetic or cutaneous feedback, known as haptics [1].

During open surgeries, doctors usually get haptic feedback directly or through the surgical tools. In minimally invasive surgeries interaction with patients via long shafts leads to the loss of some force and tactile sense. In robotic surgery systems, surgeons have to manipulate robots indirectly, which eliminates all haptic feedback [2].

Several studies [3–5] have proved that the addition of haptic feedback in the daVinci surgery robot will help to reduce the amount of surgical errors and intra-

operative injuries, which will lead to faster post-surgery recovery time and decreased rate of unsuccessful surgeries [2, 6, 7].

There are many technical challenges to overcome in order to implement the haptic feedback in the daVinci robot. One of them is getting accurate force readings from the patient side manipulator (PSM). To address this issue, we are trying to create force-sensing device, that can be easily added to the existing surgery system.

# Chapter 2

## Background

### 2.1 Teleoperated Surgical Robots

Recently, robots have started to be extensively used for surgical procedures. They allow doctors to perform these procedures with high accuracy, repeatability, and reliability, which in turn results in reducing operation time, errors and post-operation injuries. Minimally invasive surgeries are beneficial for accurate procedures with minimal access to operated organs, e.g. neurosurgery, eye surgery, cardiac surgery, intravascular surgeries and etc. Use of robots in minimally invasive procedures improves precision and reliability of surgical maneuvers [8].

Russel H. Taylor suggested classification of medical robotic systems into two categories: surgical Computer-Aided Design/Computer-Aided Manufacturing (CAD/CAM) systems and surgical assistants [9].

Surgical CAD/CAM systems are involved into the process of preoperative, intraoperative and postoperative planning, including building a patient model, registration of medical images, and monitoring of the therapy. Examples of CAD/CAM robots are ROBODOC and CASPAR systems for joint replacement surgery, LARS and JHU robots for positioning of needle guides, and systems such as Accuray Cyberknife for positioning of the radiation therapy delivery device [9].

Surgical assistants are medical robotic systems that work in cooperation with surgeons. They are divided into two classes: surgical extenders and auxiliary surgical supports. Surgical extenders are operated directly by the surgeon and are used to extend the surgeon's ability in performing an operation. Examples include master-slave manipulator systems (e.g. the daVinci system, Sensei X, Senhance) and teleoperated microsurgery systems designed for ocular microsurgery. Auxiliary surgical supports usually work side-by-side with the surgeon and perform such functions as laparoscopic camera manipulation and ultrasound probe manipulation [9].

Use of teleoperated robots in surgeries can solve many of the conventional surgery problems in terms of more precise manipulation capability, ergonomics, dexterity, and haptic feedback capability for the surgeon. They enhance dexterity by increasing instrument degrees of freedom, compensation for hand tremor, and scaling movements to transform large movements of the control grips into small motions inside the patient. Three dimensional view with depth perception gives surgeons ability to directly control a stable visual field with increased magnification and maneuverability. All of

these can extend the surgeon's ability to treat patients [8].

Today, many surgical robotic systems have been commercially developed and approved by the FDA, such as the daVinci surgical system (Intuitive Surgical, Inc., Sunnyvale, CA) (Figure 2.1), the Sensei X robotic catheter system (Hansen Medical Inc., Mountain View, CA), the FreeHand v1.2 (FreeHand 2010 Ltd., Cardiff, UK), the Invendoscopy E200 system (Invendo Medical GmbH, Germany), the Flex robotic system (Medrobotics Corp., Raynham, MA), the Senhance (TransEnterix, Morrisville, NC) (Figure 2.2), the Auris robotic endoscopy system (ARES; Auris Surgical Robotics, Silicon Valley, CA, USA), and the NeoGuide Endoscopy System (NeoGuide Endoscopy System Inc, Los Gatos, CA) [10,11].

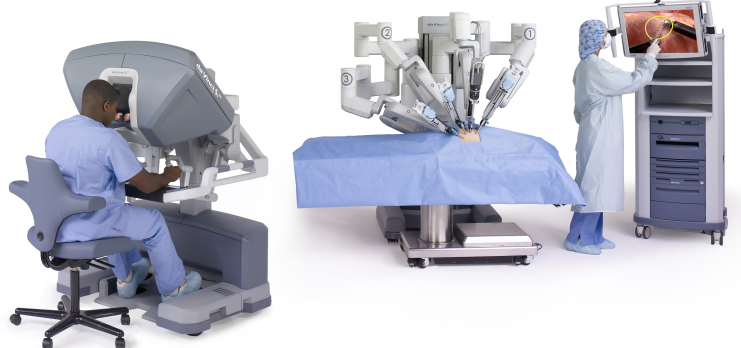


Figure 2.1: The daVinci Si Surgical System [1]

There is also a number of NON-FDA-approved platforms that are currently under development or going through clinical trials. Examples include MiroSurge (RMC, DLR, German Aerospace Center, Oberpfaffenhofen-Weling), the ViaCath system (BIOTRONIK, Berlin, Germany), SPORT surgical system (Titan Medical Inc., Toronto,

Ontario), the SurgiBot (TransEnterix, Morrisville, NC), the Versius Robotic System (Cambridge Medical Robotics Ltd., Cambridge, UK), MASTER (Nanyang Technological University and National University Health System), Verb Surgical (Verb Surgical Inc., J & J/Alphabet, Mountain View, CA, USA), Miniature in vivo robot (MIVR) (MIVR, Virtual Incision, CAST, University of Nebraska Medical Center, Omaha, Nebraska, USA), and the Einstein surgical robot (Medtronic, Minneapolis, MN) [11].

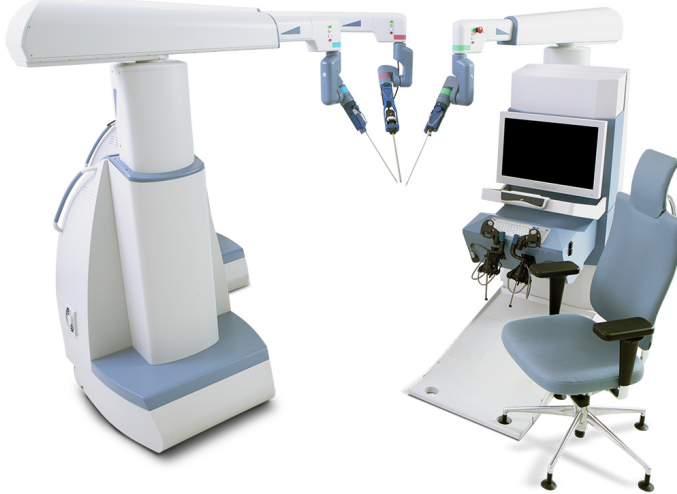


Figure 2.2: The Senhance Surgical System [12]

The daVinci surgical system is one of the most commonly used robotic surgical systems. In 2015, over 3400 systems were in use around the world. More than 3 million surgeries were performed worldwide using daVinci system [1]. The system has been approved for various types of surgeries such as cardiac, colorectal, thoracic, urological and gynecologic. However, new systems are emerging on the market, providing features that are absent currently in the daVinci System. For example, the Flex Robotic System, which consists of the flexible endoscope for laparoendoscopic

surgeries. This system is able to define a non-linear path to surgical target by advancing a flexible telescopic inner-outer mechanism with instruments inside it, whereas instruments in the daVinci system can follow only non-flexible straight path. Another example is the Senhance robotic platform, which was cleared by the FDA in 2017, that provides actual haptic force feedback, allowing the surgeon to feel forces generated at the instruments end. In addition, the system uses eye-tracking technology to move the camera at the point the surgeon is looking at, while the daVinci uses a footswitch panel to control the camera movement [11].

## 2.2 Importance of Haptic Feedback

Haptic feedback is assumed to improve surgeons' performance in robot-assisted surgeries. Several research groups tried to examine the effect of the haptic feedback on surgeons' performance in tasks including the knot tying, blunt dissection, laparoscopic cholecystectomy, and mitral valve annuloplasty repair. To assess the performance they analyzed the required time to complete surgical tasks, the peak and the mean forces applied on tissues, and rates of suture breakage.

As reported in [7], research groups [13–16] compared robotically assisted (no haptic feedback) and traditionally performed laparoscopic (has some degree of haptic feedback) surgeries in terms of required operative time and post-operative injuries rate. Meijden et al. concluded that in different types of robot-assisted surgeries the

absence of haptic feedback prolonged operative times and increased the risk of surgical errors [7]. However, there are other factors, such as surgeon experience in use of traditional laparoscopic instruments, that could explained the change in operative times.

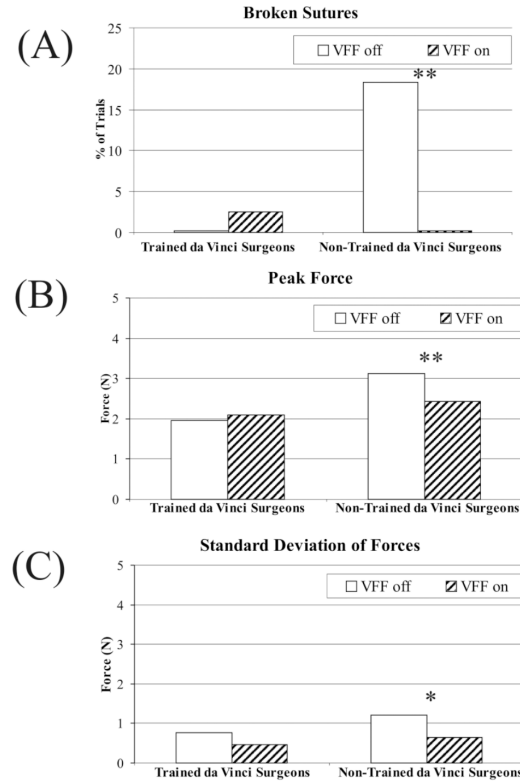


Figure 2.3: Effects of Visual Force Feedback on Robot-Assisted Surgical Task Performance [6]

In two studies, [6, 17] knot tying tasks were performed by surgeons to assess the influence of the haptic feedback. Bethea et al. reported significantly more consistent tensions applied to suture materials, without breakage, during tying with visual haptic feedback compared to without the feedback [17]. Reiley et al. implemented real time visual force feedback in the daVinci robotic system and asked two groups of surgeons

(with and without robotic experience) to tie 10 knots with and without force feedback [6]. The performance parameters they used were suture breakage rate, secureness of the knots, peak and standard deviation of applied forces, and completion times. They concluded that use of the visual force feedback resulted in lower suture breakage rates and peak forces, and decreased force inconsistencies among surgeons without robotic experience (Figure 2.3). However, among experienced daVinci surgeons it did not show any changes in performance parameters. The authors suggested that visual force feedback benefits only inexperienced robot-assisted surgeons. One of the issues with the visual force feedback (used in both studies) that it does not give much information (only color changes) about forces applied by the instruments, which diminishes haptics benefits. The difference between results of these two studies could be because in [17] the authors did not consider surgeon's experience.

Wagner et al. examined the effect of force feedback during performance of the blunt dissection task, which makes up 25-30% of the time spent on most surgeries [3]. The results of the study demonstrated that without force feedback the average force applied to the tissue increased by at least 50%, peak forces doubled and number of errors that caused tissue damage increased by over a factor of 3 (Figure 2.4). The study also shows that these results are independent of surgeons' previous experience. Also, study have shown that the rate and precision of dissection were not significantly improved with force feedback. In contrast to two previous studies, which used visual force feedback, authors used Phantom haptic interface device as the surgeon master

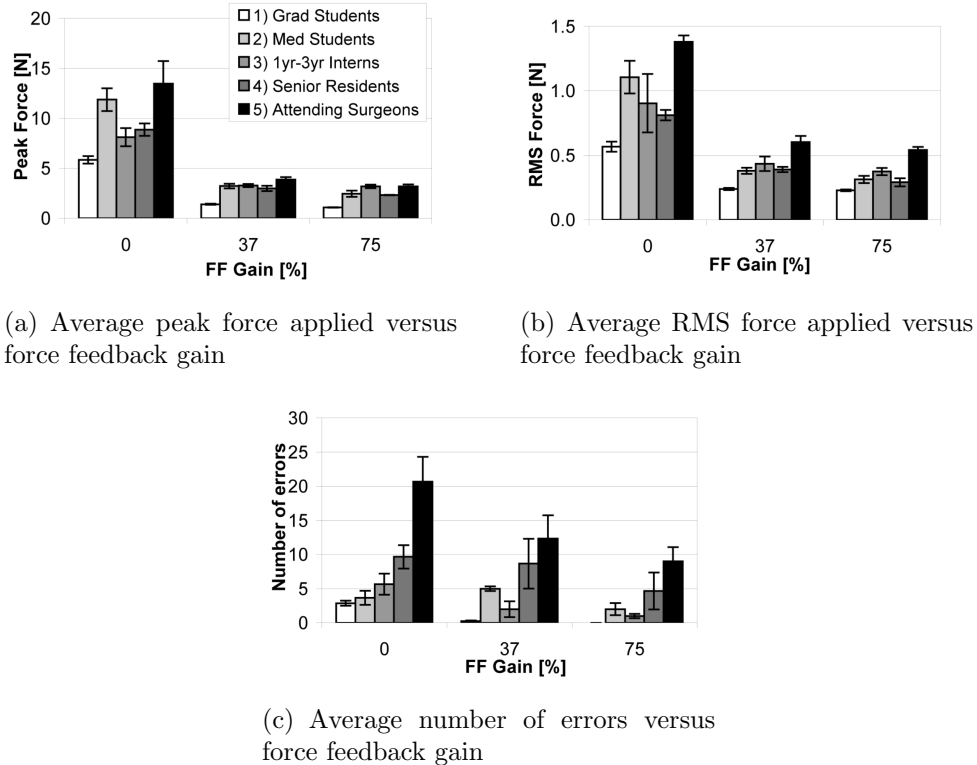


Figure 2.4: Examination of Blunt Dissection with/without Force Feedback [3]

controller, which could explain significant changes in the study results.

Yiasemidou et al. assessed the role of haptic feedback by evaluating performance of surgical trainees after simulation training [4]. They were divided in two groups and performed full procedure of laparoscopic cholecystectomy using virtual reality simulators with and without haptic feedback. The results shown that use of simulators with haptic feedback significantly reduced the time required to complete the procedure.

Currie et al. developed robotic-assisted surgical system that provides visual and direct force feedback during cardiac surgery [5]. The system measured the amount of force applied to cardiac tissue during mitral valve annuloplasty repair. The study

results have shown that the addition of both visual and direct force feedback ( $2.15 \pm 1.08$ ) causes lower peak force applied to mitral valve tissue compared to no force feedback ( $3.34 \pm 1.93N; P < 0.05$ ). In this study, authors also compared applied peak forces with only visual force feedback ( $2.16 \pm 1.67$ ) and with only direct force feedback ( $1.62 \pm 0.86$ ). Also, comparison between the performance of experts and students (with no experience in robotics-assisted surgery) have shown no statistically significant differences between the groups. The methodology of this study has been significantly improved in comparison to [17]. The authors of this study [5] used haptic devices to provide direct haptic feedback and used two study groups.

Meli et al. evaluated participants' performance on a bimanual teleoperation experiment called the peg board experiment [18]. The authors used three feedback conditions: cutaneous force feedback, complete haptic feedback provided by Omega 7 haptic interface, and auditory feedback provided by changing the repetition frequency of beep tone. They evaluated the performance in each feedback condition by comparing task completion time, the contact forces and total displacement of the rings. The comparison of these types of feedback have shown that haptic force feedback has smallest completion time, contact forces and displacement (Figure 2.5(a)). The authors also studied influence of unstable behavior of the haptic feedback by adding communication delay of 20 ms between master and slave system. The results of this study demonstrated that for the haptic force feedback all the parameters significantly increased, showing that just cutaneous force feedback allows the best performance in

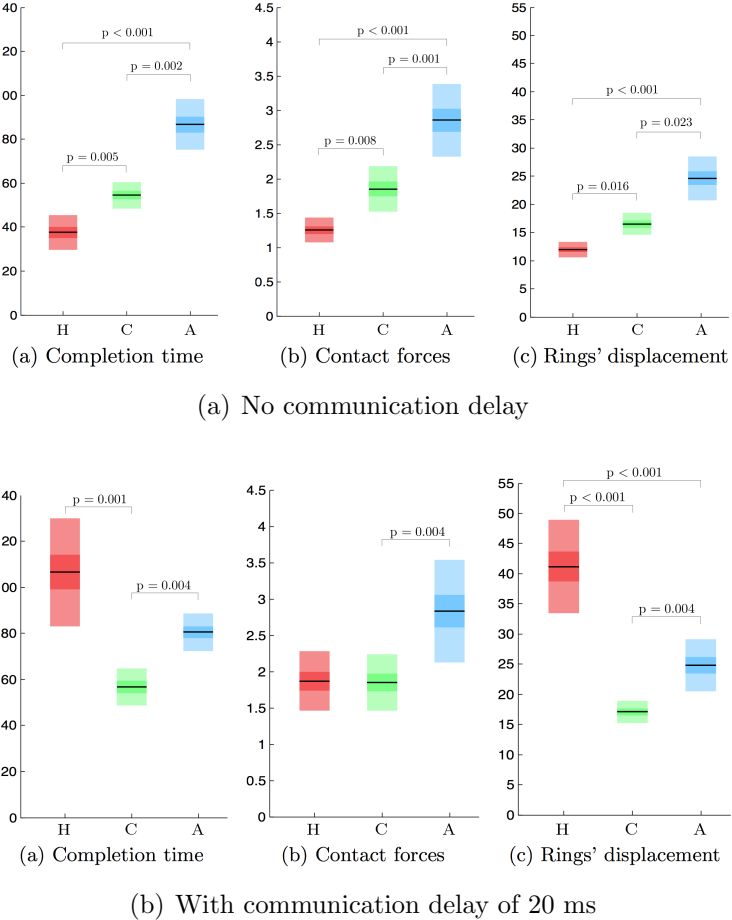


Figure 2.5: Bimanual Peg Board Experiment Results. Completion time, contact forces, and rings' displacement for the haptic (H), cutaneous (C) and auditive (A) conditions [18].

unstable conditions (Figure 2.5(b)). The authors concluded that use of the cutaneous feedback only can be more beneficial than use of full haptic feedback. However, a stable haptic feedback system without time delays could show higher performance, meaning that it is important to create stable haptic system.

The results of the studies [3–5] have shown that implementation of force feedback into teleoperated robotic systems reduces root-mean-square (RMS) and peak values

of contact forces, energy consumption, a time required for task completion and the surgical errors rate [8]. The current version of daVinci robot does not provide haptic feedback, and an addition of one would be beneficial for both patients and surgeons.

## 2.3 Current Approaches

In order to implement haptic feedback in the daVinci system, it is necessary to create force sensing method for surgical tools first. Current approaches of incorporating force sensing include placement of force sensors on surgical tools, change of instruments design and some sensorless methods.

### 2.3.1 Sensor Placement on Instrument

Hong et al. suggested measuring pulling and grasping forces at the tip of the surgical instrument by mounting strain gauges on top and bottom surfaces of each of the two flexure hinges of the forceps (Figure 2.6) [19]. RMS errors were close to 0.1 N. One of the disadvantages of this method is biocompatibility issue due to contact of sensors and wires with patient tissues, another is increased cost of each tool. Taking into account that each instrument has limited lifespan [20], it will lead to significant increase in surgery cost.

Some researchers use optical methods for the force evaluation. These methods are divided by different sensing principles they use: intensity modulation, wavelength

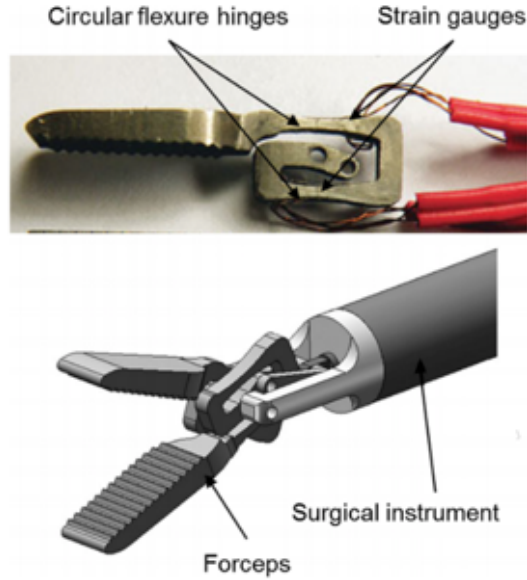


Figure 2.6: Prototype of the 2-DOF Compliant Forceps [19]

modulation, and phase modulation [21]. Peirs et al. developed 3-axial force sensor that uses light intensity modulation principle [22]. It is based on a flexible titanium structure, that deforms with applied forces (Figure 2.7). These deformations are measured through reflective measurements with three optical fibers. The method shows measurement force range 0.01 N to 2.5 N with 0.01 N resolution. The disadvantage of this method is narrow force measurement range.

### 2.3.2 New Instrument Designs

Making new surgical instrument with implemented force sensors is another way to achieve force feedback. Schwalb et al. developed the new force-sensing surgical tool, that uses a proximally located force/torque sensor (Figure 2.8) [23]. This allows

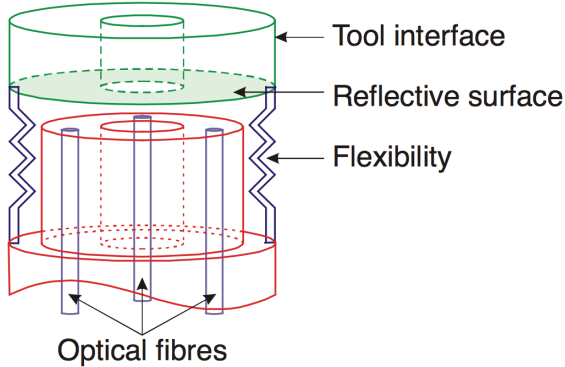


Figure 2.7: Optical Force Sensor [22]

avoiding miniaturization and sterilization issues. The method has high sensing accuracy with errors less than 0.09 N. The outer diameter of the developed tool is 12 mm. This method as well requires an increase in the tool cost, leading to higher surgery expenses.

### 2.3.3 Sensorless Methods

All sensorless estimation methods avoid drawbacks associated with biocompatibility and integration issues. There are 2 methods: vision-based force feedback and motor currents measurement method.

Aviles et al. proposed to use vision-based solution with supervised learning to estimate the applied forces [24]. After extraction of the motion geometry of the object surface, they use a deep network to learn the relationship between the extracted visual information and the applied force (Figure 2.9). The evaluated average root-mean-square error of the method is 0.02 N. The disadvantage of this methods is the

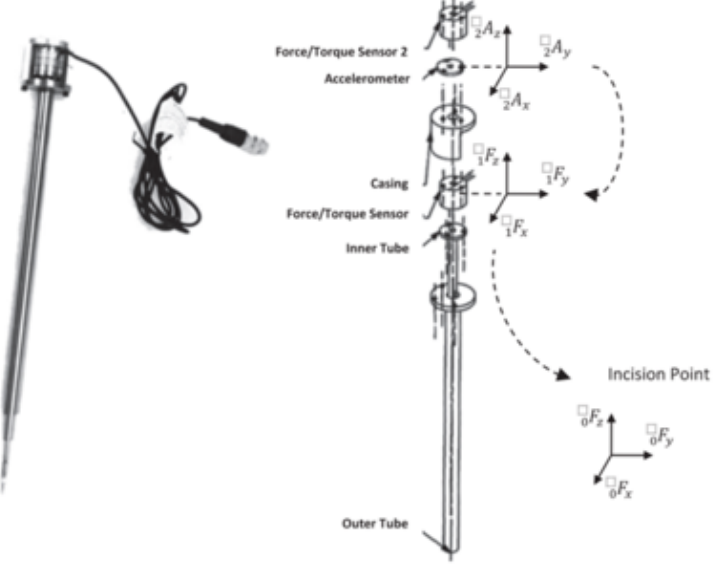


Figure 2.8: Force-Sensing Surgical Tool [23]

necessity to know object's material properties, and some materials such as bones would not visually deform. Additionally, the method has significant time delays due to computation time and is not suitable for real-time force feedback.

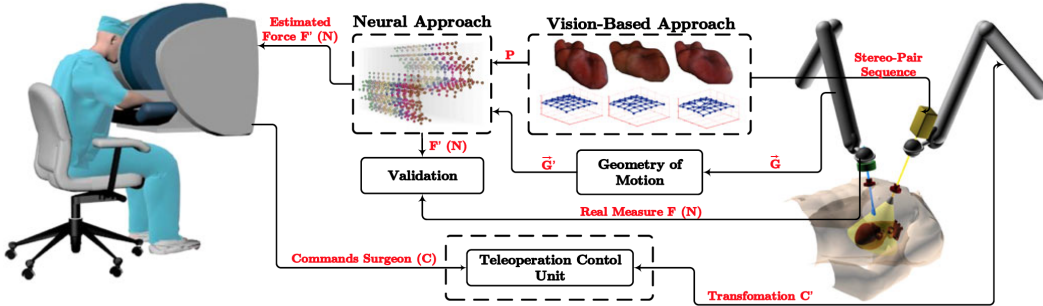


Figure 2.9: Flowchart of Vision-Based Force Estimation Approach [24]

In [25, 26], authors estimate external forces using dynamics models and motor currents from the robot. They linearly parameterized PSM dynamics model and used it to derive forces values. As a result, they implemented sensorless force estimation method and they concluded that it was feasible. Even though, the proposed method

does not show sufficient repeatability and accuracy.

## 2.4 Force Sensing Technologies

For the force sensing depending on their operating principle following types of sensors can be used: piezoelectric, strain-gauges, quantum tunneling composite pills (QTC Pills) or optical sensors [27].

- Piezoelectric sensors consist of two crystal disks with an electrode foil in between. When force is applied, an electric charge, proportional to the applied force, is obtained and can be measured. Piezoelectric sensors show small deformation when force is applied, this results in a high resonance frequency. Also, piezoelectric sensors due to their principle of operation have significant linearity error and drift [28].
- QTC Pills are flexible polymers, that have exceptional electrical properties. They are made of a nonconducting material that contains small nickel particles. In the resting state, it acts as an insulator, because metal particles are too far from each other. When it is compressed, its conductivity increases and current can pass through it [29]. QTC Pills are very sensitive and can work in wide ranged of forces. However, they have an exponential relationship between force and resistance, they are temperature sensitive and depend on charge application time. Meaning they have low accuracy and not suitable for dynamic force

measurements [30].

- In the strain gauge based force transducers, the force causes deformation and subsequent linear change in resistance. Strain gauges are usually connected to a Wheatstone bridge circuit, where the output voltage is proportional to the applied force. Strain gauge based transducers provide small individual errors (200 ppm), show no drift, and are therefore appropriate for long-term monitoring tasks. However, they are relatively big, temperature dependent, and have a lower resonance frequency in comparison to piezoelectric sensors [27, 28].
- Optical retro-reflective sensors can be used for the force measurements. Emitter and receiver of these sensors are located at the same host. The light from the emitter goes through optical fibers reaches reflector and the reflected light goes back to the receiver. An interruption of the light beam due to bending can initiate a change of the signal output. Optical sensors are rarely used for force sensing applications because measurement range and sensing accuracy of such sensors are limited [21].

On the basis of the above mentioned, piezoelectric sensors are preferable for dynamic measurements of small forces while strain gauge sensors are better when large forces are measured. In this study, strain gauges were used since they show better accuracy and long-term stability [27, 28].

## 2.5 Contributions

Force sensing devices for measuring forces in X-Y direction and one for Z-direction measurement were created. They allow getting force readings from the daVinci tools of the PSM. These devices can be easily added to the existing daVinci system. Since we have to add created device on each robot arm only, it is cheaper than placement of sensors on each separate surgical tool. Moreover, the created devices allow measuring forces faster than through the visual data processing method and could show better precision than the motor current method.

# Chapter 3

## Force Sensor Design and Characterization

This chapter sets the requirements for the force sensing system, explains the methodology behind the design of the force-sensing devices, including mechanical, electrical, and software design, and finally describes the calibration process of the created system and shows the calibration results.

### 3.1 Requirements for the System

First, from the literature review following requirements for the force sensing device were outlined:

- ***Biocompatibility.*** All the devices below the sterile adapter on the PSM are

required to be sterilized (Figure 3.1). Any device that is in direct contact with a patient needs to be biocompatible, such as the instrument shaft and the cannula.

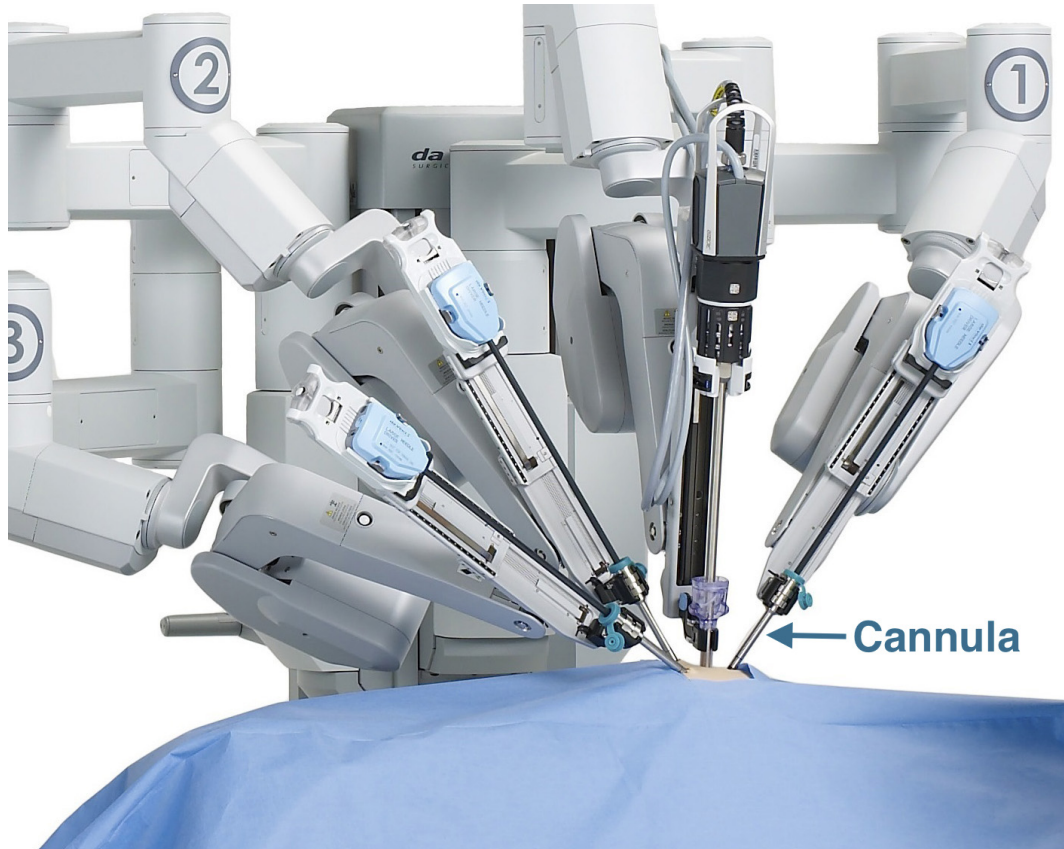


Figure 3.1: Cannula Placement Inside a Patient on the daVinci Si System [1]

- **Force range.** One of forces that have to be measured is maximum safe value before the instrument shaft is overloaded and damaged, if the force goes beyond that range it can be used to trigger safety alert. Friedman et al. analyzed instances of the daVinci instrument failures [31] and concluded that majority of failures were of the instruments wrist or tool tip. Additional studies have to be done to find the magnitude and the direction of the forces that caused these failures. Max value of the force applied during surgeries corresponds to

retractor forces (up to 10 N) [32]. Majority of people perceive a force of 11N to be a solid object [33]. In order to meet these requirement the designed device needs to measure forces between 0 N and at least 11 N, but the maximum level could be higher depending on the threshold for the tool damage.

- ***Sensitivity and accuracy.*** The device needs high resolution (at least  $0.05N$ ) so user can feel small differences between materials and give accurate readings ( $error < 0.1N$ ) [33].
- ***Bandwidth.*** Because the device is used for real-time haptic feedback, the minimum rate for data acquisition is 0.5 kHz [34] and ideally it should be close to 1 kHz.
- ***No restriction of motion range of the device.*** The forces should be measured in three directions independently from each other. At the same time, the tool should freely rotate and change the depth of insertion.
- ***Linearity.*** Calibration curve of created sensors should be linear.
- ***Device modularity.*** Force-sensing devices should be designed so they can be easily added to the existing system and fit daVinci cannula and sterile adapter. Also, the sensors should use ROS interface due to its inter-process communication ability and modularity [35].

## 3.2 Force Measurement

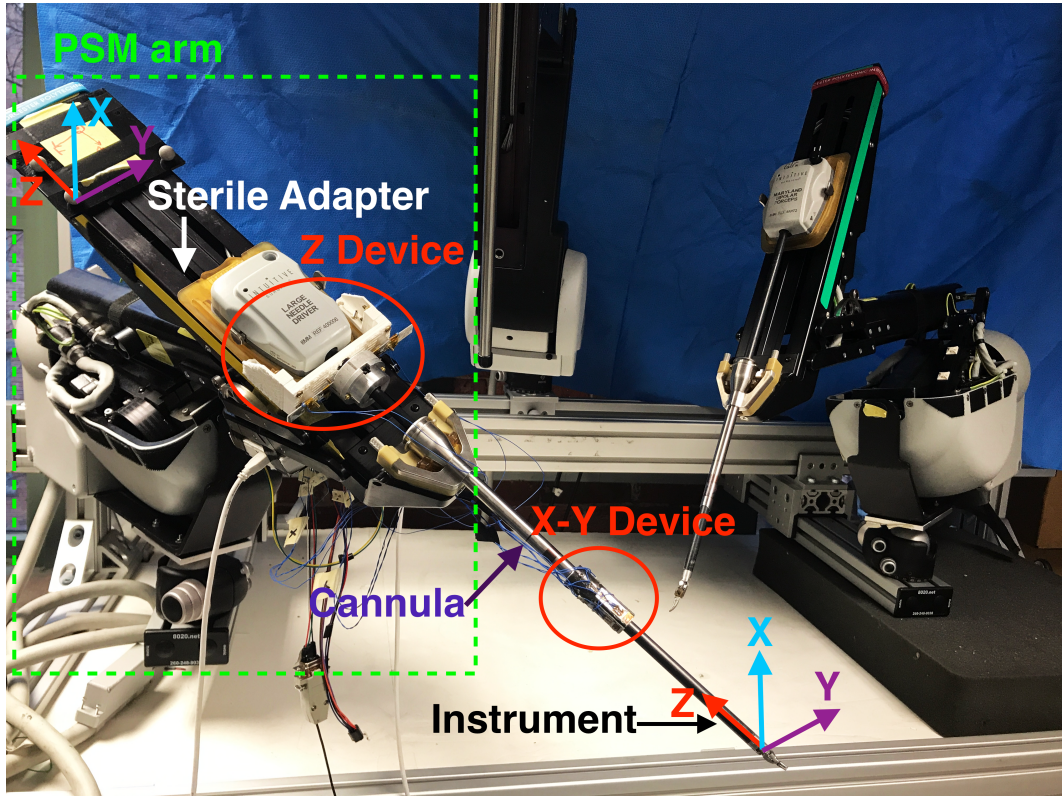


Figure 3.2: Developed Force Measuring System Attached to the PSM. The daVinci instrument is inserted in the sterile adapter of the PSM arm. Z Device is attached to the sterile adapter. XY Device is press-fitted on the cannula end.

A block diagram of the created system for 3-DOF force measurement is shown in Figure 3.3. Forces that applied on the end of the surgical tool are measured using strain gauges, which change their resistance with force. Using created printed circuit boards (PCBs), these resistance changes are measured and published within robot operating system (ROS). At the same time, we measure a current joint position of the tool, which is needed for the force calibration. The position data and data from PCBs are used to find values of the force in X, Y, Z directions (Figure 3.2).

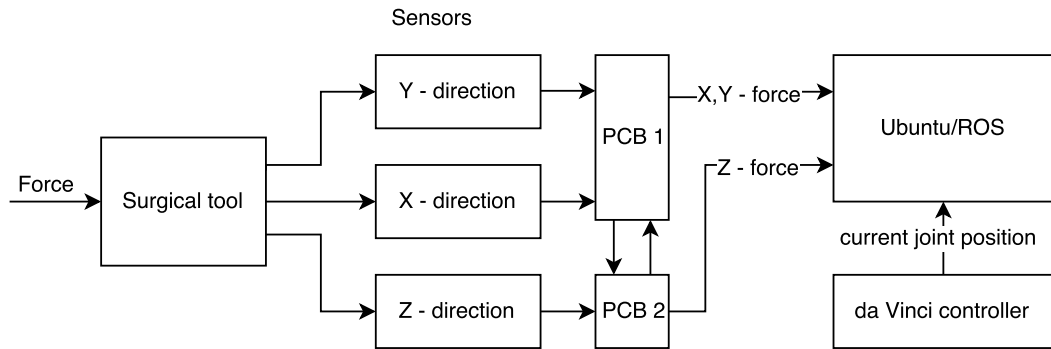
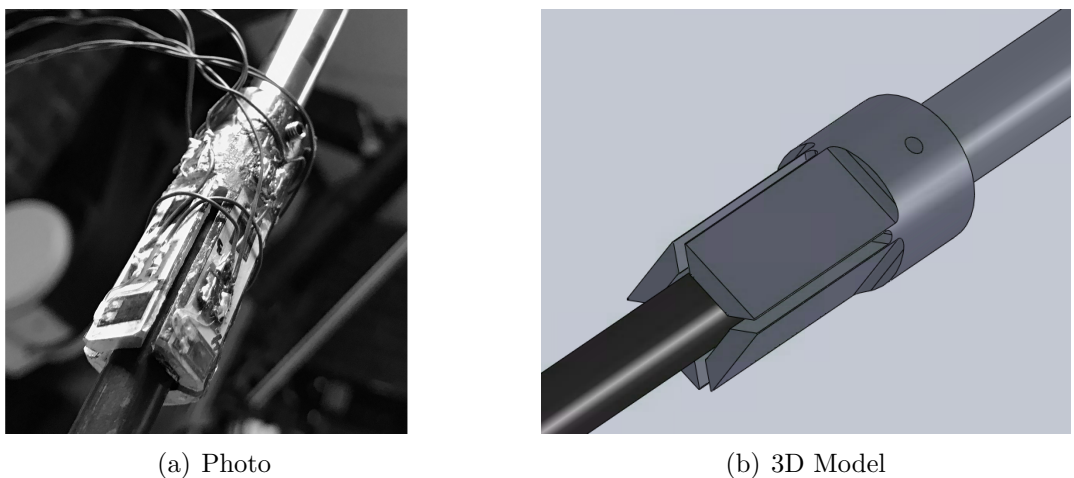


Figure 3.3: Block Diagram

### 3.3 Mechanical Design

This chapter describes mechanical design of two sensors, one for measurement of the X-Y component of the force, and another for the measurement of the Z-component of the force.

#### 3.3.1 X-Y Device



(a) Photo

(b) 3D Model

Figure 3.4: XY-direction Force Feedback Sensor

The XY-device consists of one sleeve and one set screw. We manufactured sleeve using Aluminum 6061 Alloy. The manufactured sleeve is placed on the cannula end and is fixed with a set screw on the top (Figure 3.4). The sleeve was manufactured slightly wider than the cannula to compensate tolerances in cannula sizes.

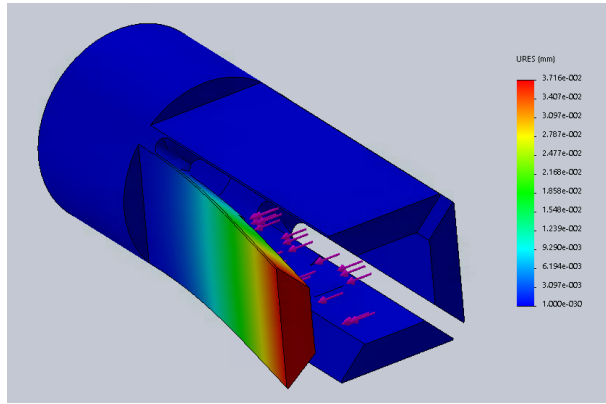
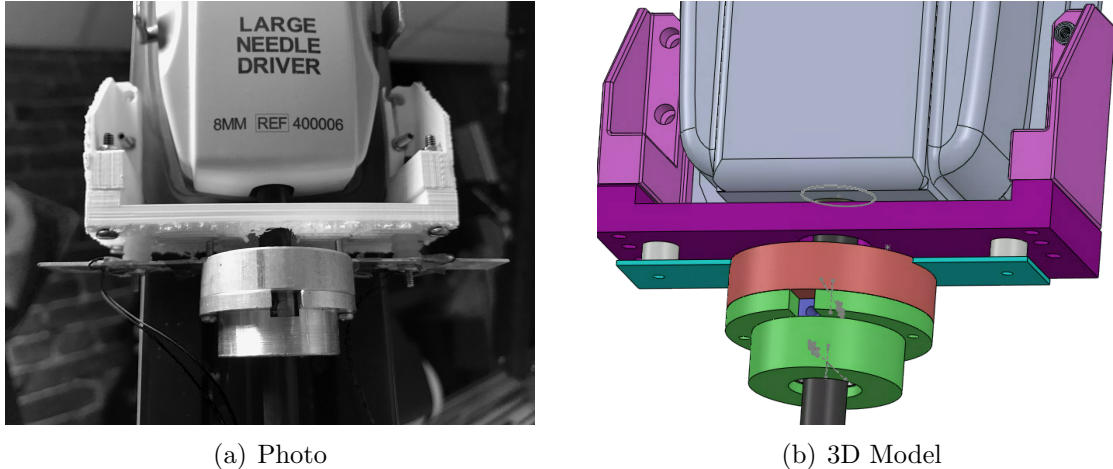


Figure 3.5: Displacement of the XY Device

In order to get accurate readings maximum displacement of the sleeve sides should prevent shaft from hitting the cannula. It means that it should be less than distance between the cannula and the instrument shaft  $d = (d_{can} - d_{shaft})/2 = (8.75 - 8.4)/2 = 0.175$  mm, where  $d_{can}$  is inner diameter of the cannula and  $d_{shaft}$  is outer diameter of the shaft. From the Solidworks simulation (Figure 3.5), maximum displacement is 0.037 mm, which is in appropriate range.

### 3.3.2 Z Device

Z-device principle of work based on low rigidity in the connection between the sterile adapter and the surgical instrument, which allows movement of the instrument



(a) Photo

(b) 3D Model

Figure 3.6: Z-direction Force Feedback Sensor

for approximately 0.3 mm in Z-direction. By designing the Z-Device to be more rigid than this connection, we can support the force in Z-Device rather than the sterile adapter.

Z-device (Figures 3.6 - 3.7) consists of attachment to the sterile adapter, 2 thrust ball bearings, three rings, plate, and two cylindrical spacers. Three rings and two ball bearings are used to transfer only z-directional forces further to the plate and keep the ability of the shaft to rotate. The ring in the center is in direct contact with the instrument shaft, two outer rings are for the push and pull forces transfer. The plate experience maximum strain and all strain gauge sensors are mounted on it. Two cylindrical spacers are used to give plate space to move and they are mounted on the attachment plate. The attachment plate consists of three plates, they are press-fitted on the sterile adapter and fixed with four set screws.

Three rings and plate were manufactured with Aluminum Alloy 6061, attachment

parts were 3-D printed, fasteners were used as spacers.

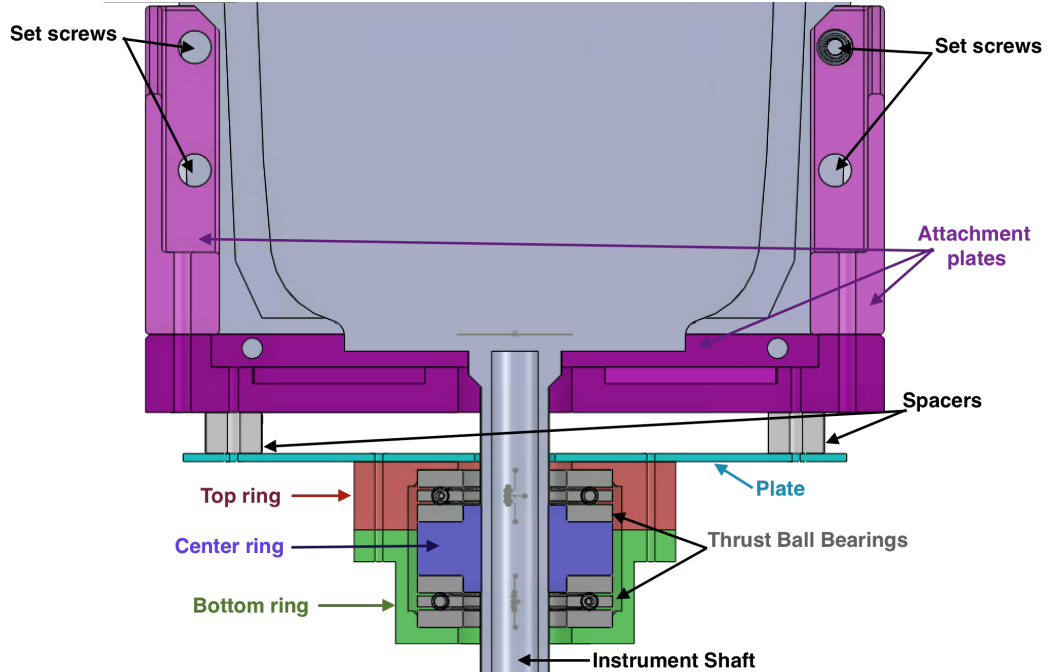


Figure 3.7: Z-direction Force Feedback Sensor (Section View). Center ring in direct contact with instrument shaft, the contact was created using set screw. Thrust ball bearings are used to transfer only Z-component of the force. Top and bottom rings transfer push and pull forces to the plate. Spacers are used to give a space for plate to move. Set screws are used to fit attachment plates on the sterile adapter

## 3.4 Sensor Selection and Placement Optimization

This section describes the selection of strain gauges and their mounting locations, and the process of their attachment to the devices (described in previous Section 3.3).

### **3.4.1 Sensor Placement Optimization**

In order to accurately measure forces, the strain gauges should be placed in the area with the highest strain. A finite element analysis was done in Solidworks to find strain distribution and assess the better mounting location of the strain gauges on the created devices. In order to run finite element analysis material properties, such as elastic modulus, Poisson's ratio, and density are necessary to know. Devices material is aluminum 6061, which has elastic modulus 68.9 GPa, Poisson's ratio 0.33, and density 2700 kg/m<sup>3</sup> [36]. Since the shaft and cannula materials are unknown, in order to run finite element analysis their elasticity modulus and density were found experimentally.

#### **3.4.1.1 Elastic Modulus Measurements**

Elastic Modulus of the shaft and the cannula were found experimentally (Figure 3.8). One end of the observing sample (shaft/cannula) was fixed and the force was applied to the other end. We used weights 250g for the shaft and 555g for the cannula to apply forces. The deformation caused by forces was detected with a dial indicator. The experiment was repeated 5 times, average displacement value was used to calculate elastic modulus. Results are shown in Table 3.1.

Elastic Modulus was found using the following equation:

$$E = \frac{FL^3}{3\delta I} \quad (3.1)$$

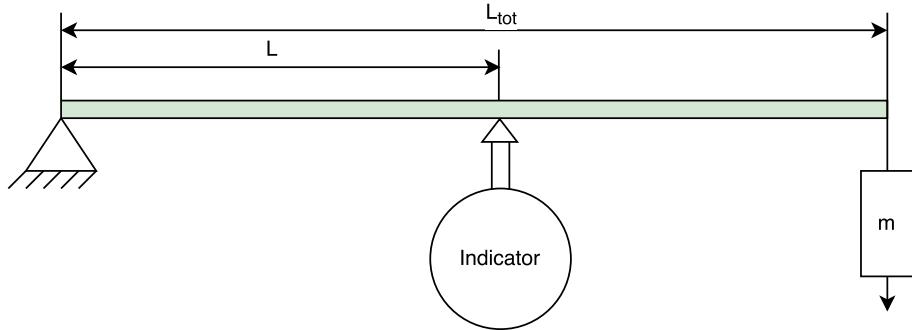


Figure 3.8: Setup to Measure Elastic Modulus

where  $F$  - force,  $L$  - length from the fixed point to indicator,  $I$  - area moment of inertia,  $\delta$  - displacement.

Area moment of Inertia:

$$I = \frac{\pi(d_o^4 - d_i^4)}{64} \quad (3.2)$$

where  $d_o$  - cylinder outside diameter,  $d_i$  - cylinder inside diameter.

Force acting on indicator:

$$F = \frac{L_{tot}}{L} mg \quad (3.3)$$

where  $L_{tot}$  - total length of the object,  $m$  - mass of the weight,  $g$  - gravitational constant.

Experimentally found the mean value of elastic modulus of the shaft is equal to 44.31 GPa with standard deviation (SD) 1.86 GPa, an elastic modulus of the cannula is 63.92 GPa with SD 2.97 GPa.

Table 3.1: Elasticity Modulus Measurement Data

Component	$d_o$ , mm	$d_i$ , mm	$I$ , $\text{mm}^4$	$m$ , g	$F$ , N	$L$ , mm	$L_{tot}$ , mm
Shaft	8.4	6	$1.808 \cdot 10^{-10}$	250	3.25	276.2	366.8
Cannula	10.54	8.75	$3.181 \cdot 10^{-10}$	555	6.011	95.5	105.55
Component	$\delta \pm SD$ , mm		$E \pm SD$ , GPa				
Shaft	$2.856 \pm 0.123$		$44.31 \pm 1.86$				
Cannula	$0.086 \pm 0.004$		$63.92 \pm 2.97$				

### 3.4.1.2 Density Measurements

Density was found using following equation:

$$p = \frac{m}{V} \quad (3.4)$$

where  $m$  - mass,  $V$  - volume.

Weight was measured using mechanical scale. Volume of the shaft was found by following equation:  $V = \pi h(r_o^2 - r_i^2) = 4.36 \cdot 10^{-5} \text{ m}^3$ . Volume of the cannula was found using water displacement method. Shaft material density is  $473 \text{ kg/m}^3$ , cannula material density is  $5523 \text{ kg/m}^3$ .

### 3.4.1.3 Simulation Results

The mounting location of the active strain gauges should be under the greatest amount of strain. From the Figure 3.9, it can be seen that strain gauges for X-Y direction device should be mounted on the area shown green, that corresponds to strain value approximately equal to  $1.5 \cdot 10^{-4}$ . Passive strain gauges, that will be used only for temperature compensation, will be placed in the blue area perpendicular to

the active strain gauges.

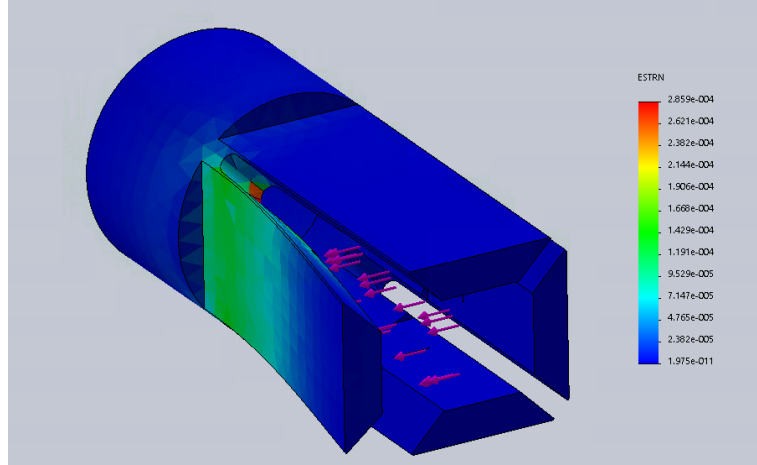


Figure 3.9: Strain in the Device to Measure Forces in X-Y Direction

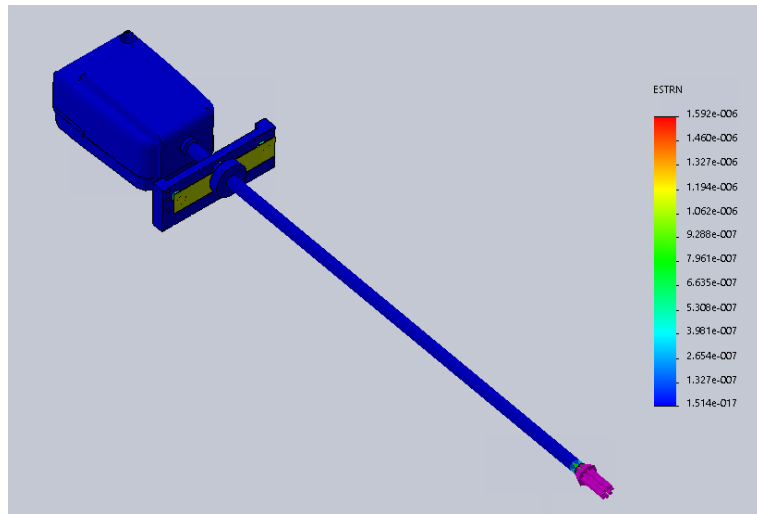


Figure 3.10: Strain in the Device to Measure Forces in Z Direction

For Z-direction measurement forces (Figure 3.10), the area shown with yellow-green color under the highest strain. On both sides and both ends of this plate strain gauges should be placed to form the full bridge.

All material properties used for simulations are listed in Table 3.2.

Table 3.2: Material Properties

Component	Elastic Modulus, GPa	Density, kg/ m <sup>3</sup>
Shaft	44.31	473
Cannula	63.92	5523
Sleeve	68.9	2700

### 3.4.2 Strain Gauge

This section describes the selection criteria of the strain gauges.

According to the manual for strain gauge selection provided by Vishay Micro-Measurements, in the created sensors the strain gauge needs to have following parameters:

- One of the requirements for the system is unidirectional force measurements. Single grid sensors are used for these purposes.
- Sensors need to be encapsulated with pre-attached leads, since they are easier to mount.
- Sensors with STC (self-temperature-compensation) show smaller temperature dependence.
- Length of the strain gauge depends on the maximum strain in the system. From the FEM analysis, the maximum strain on the created device is  $1.5 \cdot 10^{-4}$ , in case of 11 N load with the maximally opened shaft. From the literature, strain gauges length should be more than 5% of maximum strain, hence, the minimum

length of the strain gauge should be 0.0075 mm.

- Gauge Factor (GF) for strain gauges usually is 2. According to the formula (3.5) strain gauge with resistance  $120 \Omega$  have maximum change in resistance equal to  $0.036 \Omega$ , and  $350 - 0.105 \Omega$ :

$$\Delta R = GF \cdot R \cdot \varepsilon \quad (3.5)$$

where  $GF$  - gauge factor,  $R$  - resistance,  $\varepsilon$ - strain.

The selected strain gauges, used in the device, are BF350-3AA High-Precision Strain Gauges with resistance  $350 \pm 0.1\Omega$ , GF is 2, single grid, encapsulated with pre-attached leads. Bill for strain gauges is provided in Appendix B.

### 3.4.3 Installation of Strain Gauges

Application of strain gauges was done following the manual provided by Vishay Micro-Measurements [37].

First, the working surface (glass) and tweezers were cleaned with Neutralizer 5A (Figure 3.11). After that shaft surface preparation was started, using solvent degreaser GC-6 Isopropyl Alcohol. A gauge layout was then applied with a 4H drafting pencil. The surface was then conditioned with Conditioner A and the extra liquid was wiped with gauze. Finally, the surface was then neutralized with M-Prep Neutralizer 5A [37].

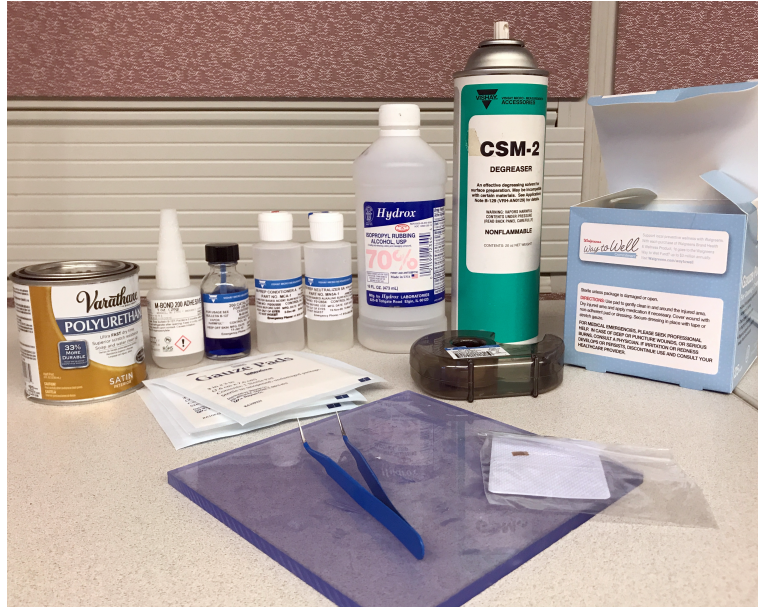


Figure 3.11: Materials for Strain Gauge Application

The strain gauges were first placed on the glass and then transported using mylar tape onto the instrument surface. A thin layer of catalyst was applied to the strain gauge and given one minute to dry. Then adhesive M-BOND 200 was applied on the surface, the pressure was applied on the tape for one minute, then two more minutes to let it dry before the tape was removed. Then leads soldering was done by application of pads, and soldering them with thin wires [38].

The methodology of the strain gauge application is more specifically described in [37]. In compliance with the application guide, the same materials and technique can be used to apply strain gauges on different materials (metals, plastics). Bill of materials for strain gauge application is provided in Appendix B.

## 3.5 Electrical and Software Design

This section describes the printed circuit board (PCB) created to detect and amplify changes in sensor readings, the microcontroller software to sent sensor readings within ROS, and the ROS architecture used to find forces from sensor readings.

### 3.5.1 Circuit design

PCB was developed to amplify sensor readings, digitize them and sent within ROS. Signal waveforms and the block diagram of this PCB are shown in Figure 3.12.

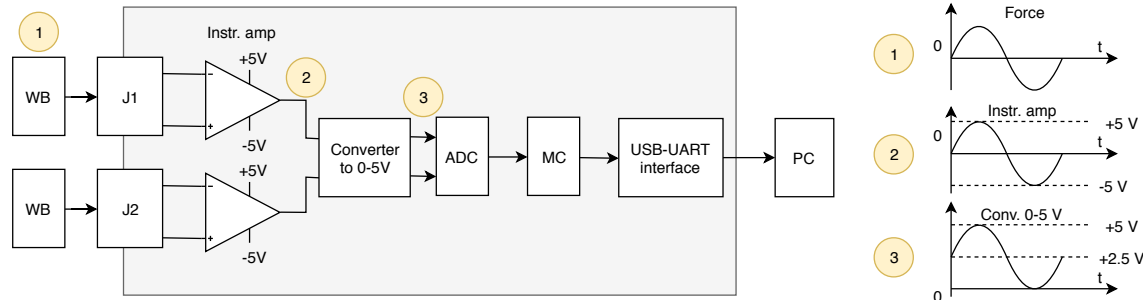


Figure 3.12: Block Diagram of the Circuit

Wheatstone bridge circuit is used to detect small resistance changes in the strain gauges. Full-bridge configuration of the circuit was used, because it gives temperature insensitivity (all sensors will change their output with temperature change) and high strain sensitivity. Four strain gauges are connected to form a Wheatstone bridge circuit. In Figures 3.13 - 3.14 placement of strain gauges (1-4) and their Wheatstone bridge configurations are shown for both devices. Strain gauges deform due to applied forces (1) in Figure 3.12, and it causes the voltage change on Wheatstone bridge. The

output signal from the Wheatstone bridge goes to the instrumentation amplifier (2).

Since ADC can convert only positive voltage, voltage converter changes voltage range of the output signal from ( $-5V$  to  $+5V$ ) to ( $0V$  to  $+5V$ ) range (3). That signal is converted to the digital signal with 16-bit ADC, which communicates with the microcontroller via SPI interface. The output signal is transferred to the computer via USB.

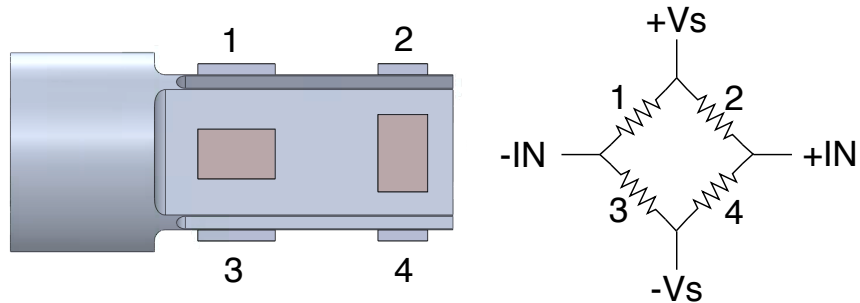


Figure 3.13: Wheatstone Bridge Configuration of the XY-device

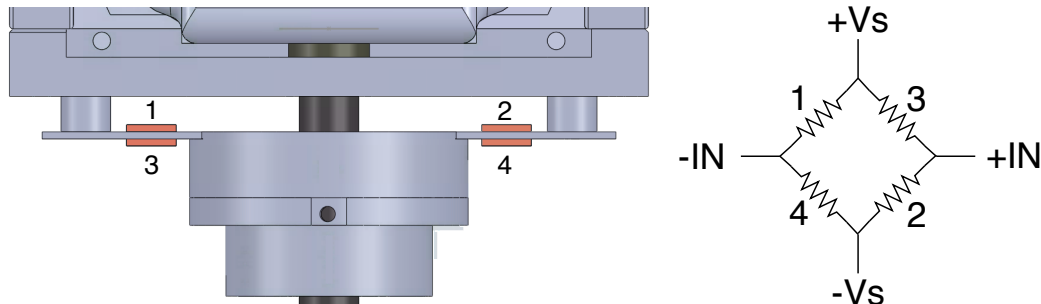


Figure 3.14: Wheatstone Bridge Configuration of the Z-device

Using Altium Designer 15.1 the PCB design was developed and manufactured at Advanced Circuits [39] (see more design details in Appendix A, bill of materials is in Appendix B).

In the developed PCB (Figure 3.15) trimpots are used for calibration of the in-

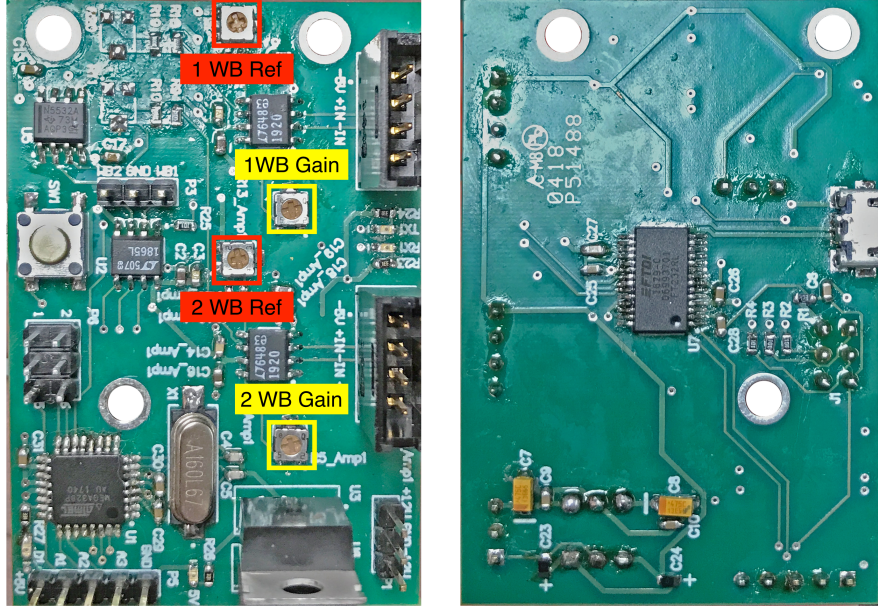


Figure 3.15: Manufactured PCB

strumentation amplifier gain (shown yellow) and change of reference voltage (shown red).

Instrumentation amplifier gain change is needed to set up appropriate measuring force range (0-11 N). During calibration, when 11 N applied on the tool end, the output signal (that goes to ADC) should be smaller than 4 V. When the same force applied in the opposite direction, the output signal should be bigger than 1 V.

Reference voltage change is used for the compensation of Wheatstone bridge unbalance caused by strain gauge resistance tolerances. During the calibration, it should be tuned until it gives the output signal close to 2.5 V when no forces applied on the device.

### 3.5.2 Noise Analysis

Fast Fourier transform (FFT) waveform analysis of the noise signal on PCB outputs (before signal goes to ADC) was performed using Tektronix MSO 4034 Mixed Signal Oscilloscope. The oscilloscope automatically applied the Hanning window, which has good frequency resolution and reduced spectral leakage [40].

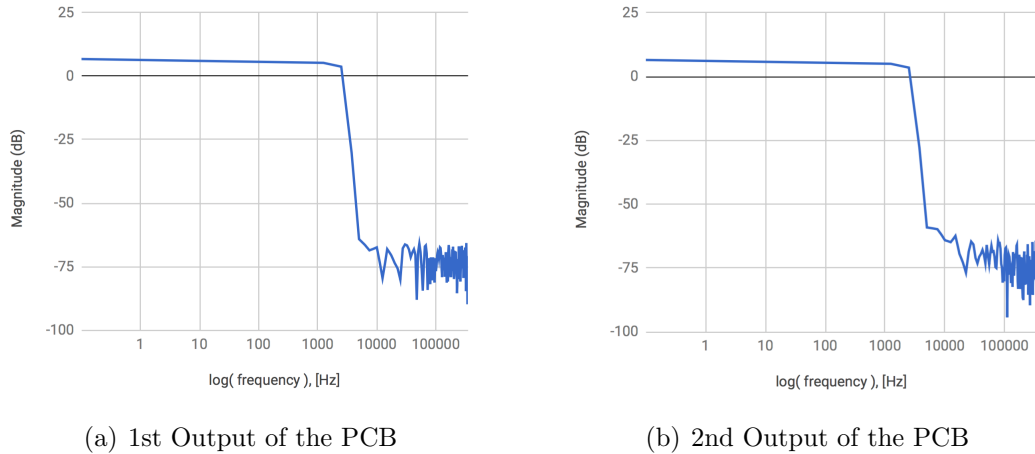


Figure 3.16: FFT Analysis Results

The signal frequency from the force sensor should be in the range of (0 to 1 kHz). From the FFT analysis results (Figure 3.16) it can be concluded, that the noise frequency is in range (2.5 kHz and higher) with amplitude (-50 mV to 70 mV) for both channels. That means low pass filter with cutoff frequency 2 kHz should be applied to the output signal. It was decided to use data averaging due to its simplicity of implementation and small time delays. It is an equivalent of low pass filtering that compensates the high-frequency noise [41].

### 3.5.3 Microcontroller Software

Microcontroller ATMEGA328P is used in the developed PCB for data acquisition, filtering, and sending to ROS. The microcontroller has open-source packages for serial communication with ROS. The microcontroller is programmed to initialize ros nodes with names "adc\_xy" for XY-device and "adc\_zlc" for Z-device. The master-slave communication is created between X-Y and Z- devices for data acquisition synchronization by sending start conversion signals between two PCBs. When one of the devices gets the signal it starts to communicate with ADC though SPI interface (Figure 3.17) [42]. The acquired data (5.8 kHz) is filtered from the high-frequency noise by averaging of the 5 most recent readings. And the filtered data is published through the serial port with the baud rate 115200 bits per second.

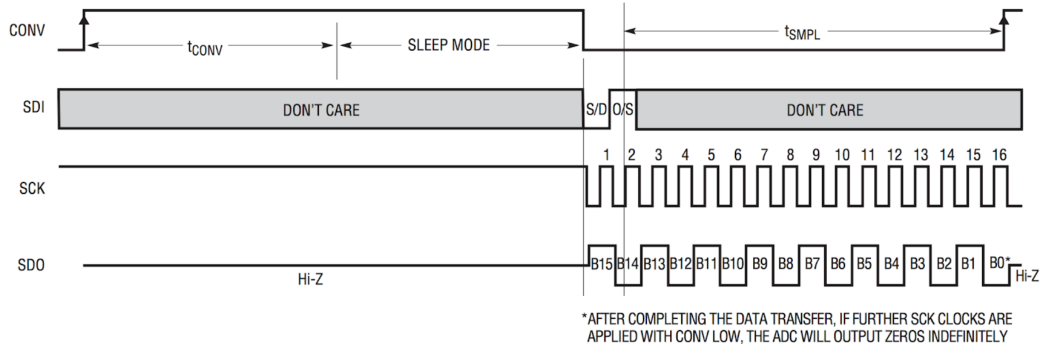


Figure 3.17: LTC1865 Operating Sequence [43]

### 3.5.4 ROS Architecture

Figure 3.18 shows the ROS architecture of the developed system. In the python script we create a *force\_feedback* node. The node is subscribed to X, Y, Z ADC data acquired form sensors and position of the sterile adapter from the daVinci controller. These data are used to find forces. The calculated forces (*force\_x*, *force\_y*, *force\_z*) are then published.

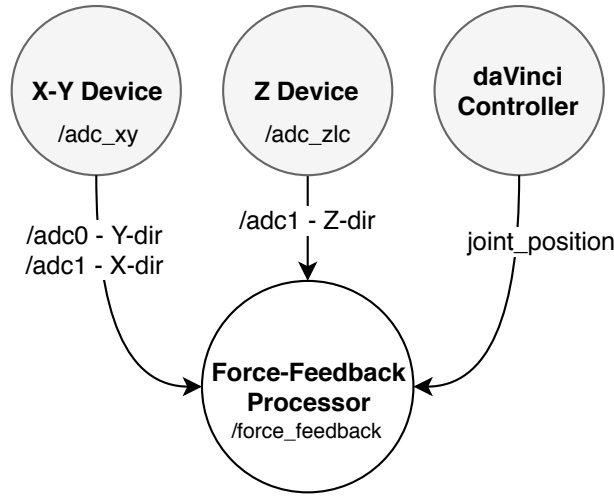


Figure 3.18: ROS Architecture

The program calculates magnitude of the forces in X, Y, Z directions using the calibration equation:

$$F = \frac{adc_{data} - b}{a} \quad (3.6)$$

where  $b$  is the constant equal to ADC reading when  $F = 0$ ,  $adc_{data}$  is current sensor reading in corresponding direction, and  $a$  is linear function of sterile adapter position:

$$a = c \cdot position + d \quad (3.7)$$

where  $c$  and  $d$  are constants found during calibration and *position* is the position of the sterile adapter (it will be discussed in the Section 3.7.2).

Z-device readings does not depend on the position of the sterile adapter. Hence,  $a$  has a constant value for Z-device.

## 3.6 Calibration

The calibration system and calibration process of the created devices are described in this section. The described system can be used to calibrate other similar force sensors.

### 3.6.1 Calibration System

In order to find parameters of the calibration equation (3.6), the calibration system was developed (Figures 3.19 - 3.20). As shown in the figure 3.19 the load cell and Polaris optical tracking system are used to find "actual" force applied to the tool end. The load cell is used to find the magnitude of the applied force and the optical markers (4-5) to find the direction of the force.

The calibration of the device starts with calibration of the load cell. The daVinci tool is inserted in the sterile adapter. The force readings depend on the position of the sterile adapter, meaning that the force/sensor readings curve should be found for different positions of the adapter. Finding the curve for only two positions would

be enough, because the correlation between the curve and position is linear, as the equation (3.7) shows.

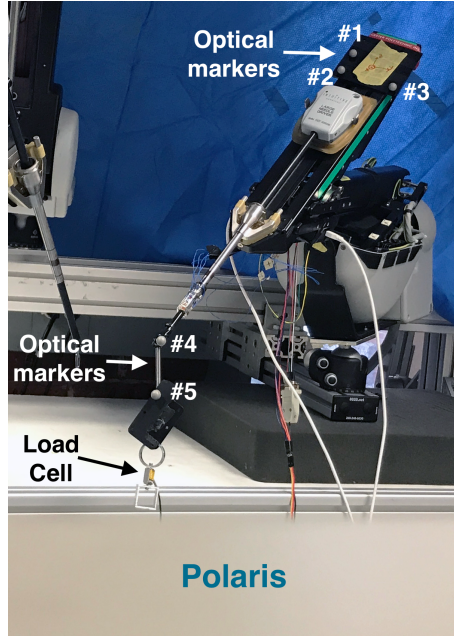


Figure 3.19: Photo of the Calibration Setup (from the prospective of the Polaris)

Before starting a data collection, the PSM joint of the sterile adapter is fixed in the position 1. After fixing the adapter, in order to transform Polaris camera frame to the robot frame, the transformation matrix should be found. For this purpose, three optical markers (1-3) are attached to the PSM. Z-direction vector corresponds to the vector formed by optical markers (2-1), Y-direction vector is formed by optical markers (2-3). X-direction vector can be found as a cross product between these two vectors:

$$\mathbf{X} = \mathbf{Y} \times \mathbf{Z} \quad (3.8)$$

The transformation matrix  $\mathbf{T}_c^r$  is found using coordinates of the  $\mathbf{X}$ ,  $\mathbf{Y}$ ,  $\mathbf{Z}$  vectors

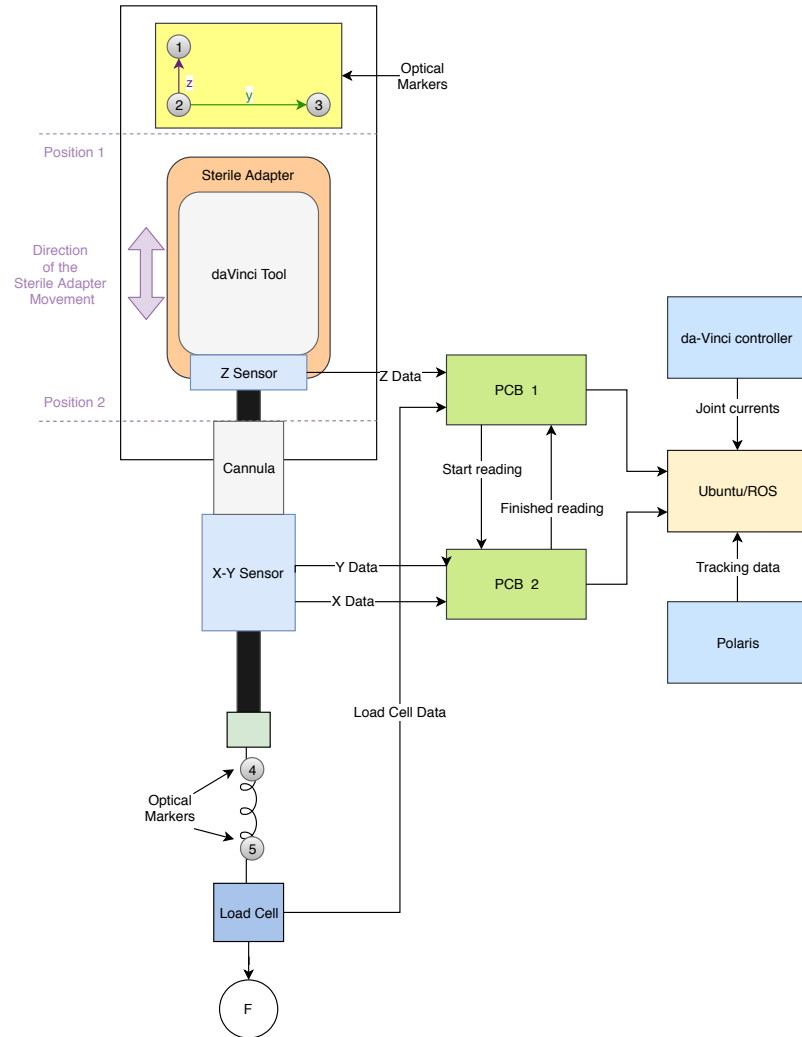


Figure 3.20: Block Diagram of the Calibration Setup

and coordinates of the optical marker (2) defined as an origin vector.

$$\mathbf{T}_c^r = \begin{bmatrix} X_x & Y_x & Z_x & x_0 \\ X_y & Y_y & Z_y & y_0 \\ X_z & Y_z & Z_z & z_0 \\ 0 & 0 & 0 & 1 \end{bmatrix} \quad (3.9)$$

After finding the transformation matrix, the data collection starts. Polaris publishes coordinates of the optical markers (4-5). These coordinates are transformed to the robot frame:

$$\mathbf{P}_r = \mathbf{T}_c^{r-1} \cdot \mathbf{P}_c \quad (3.10)$$

where  $\mathbf{P}_r$  - coordinates of the marker in the robot frame,  $\mathbf{P}_c$  - coordinates in the camera frame.

The unit vector of the applied force is found in the robot frame:

$$\mathbf{U} = \frac{\mathbf{P}_5 - \mathbf{P}_4}{|\mathbf{P}_5 - \mathbf{P}_4|} \quad (3.11)$$

where  $\mathbf{P}_5$  is the position of the optical marker (5),  $\mathbf{P}_4$  is the position of the marker (4), they both are in the robot frame.

The vector of the applied force in the robot frame can be found:

$$\mathbf{F} = F_m \cdot \mathbf{U} \quad (3.12)$$

where  $F_m$  is the force magnitude found using the load cell. At the same time data from X, Y, Z sensors is collected. The collected data is used to find calibration equation parameters.

### 3.6.2 Calibration of the Load Cell

The calibration of the load cell is a part of the calibration process of the created device. The block diagram of the setup for the load cell calibration is shown in Figure 3.21. The force  $F$  was applied on the load cell using weights, its value:

$$F = mg \quad (3.13)$$

where  $m$  is mass of the weight and  $g$  is the gravitational constant.

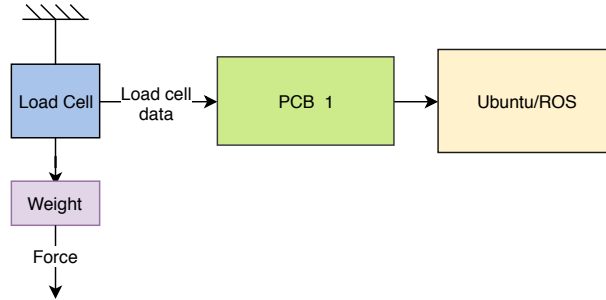


Figure 3.21: Block Diagram of the Load Cell Calibration Setup

The calibration equation for the load cell is following:

$$F_m = adc_{lc} * a_{lc} + b_{lc} \quad (3.14)$$

where  $adc_{lc}$  is acquired ADC data from the load cell;  $a_{lc}$  and  $b_{lc}$  are constants of the linear equation.

Calibration resulted in parameters of the linear equation being  $a_{lc} = -4.95 \cdot 10^{-4}$  and  $b_{lc} = 16.6$ . These values were used to find the magnitude of the applied force on

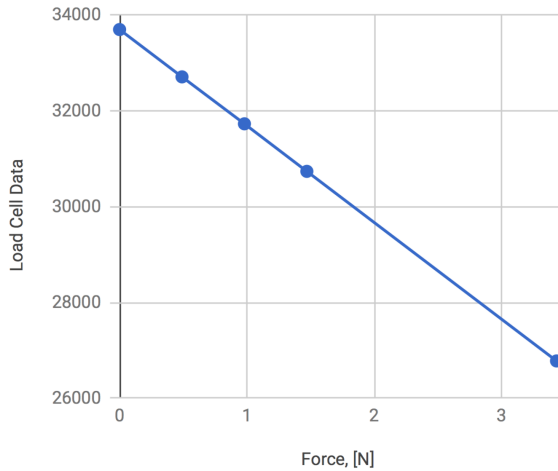


Figure 3.22: Load Cell Calibration Result

the tool end during X-Y and Z devices calibration.

## 3.7 Results

This section provides the calibration results for the created sensors. And also the results from the study relating the sterile adapter position to the coefficients of the calibration curves.

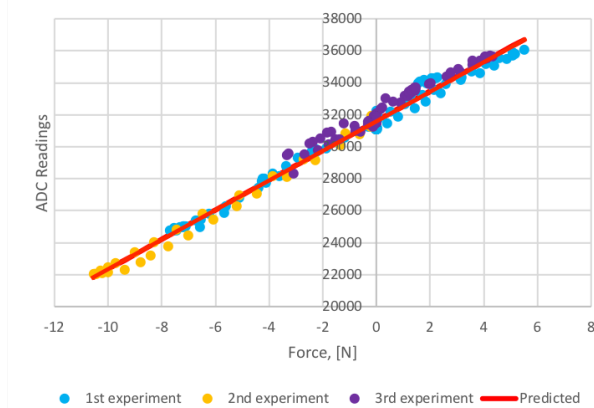
### 3.7.1 Calibration Results

The calibration results are shown in Figures 3.23 - 3.24, where blue dots are sensor readings and the calibration function shown as a red line. The results for the Z device are presented in Figure 3.24(a). As an alternative method to evaluate forces exerted in a Z-direction we used joint effort readings (Figure 3.24(b)). This method is simple

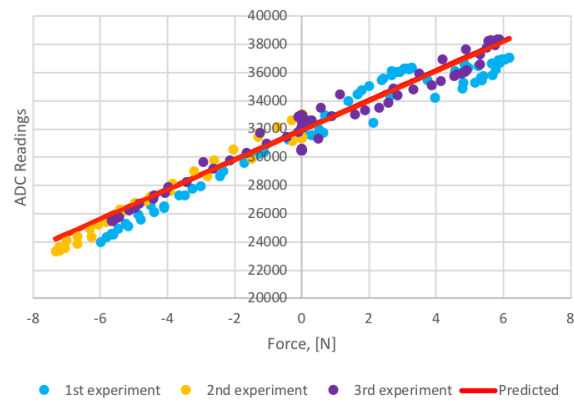
to implement by subscribing to the joint efforts of the daVinci controller and can be used for comparison with created Z-device.

The performance of the created devices was evaluated using standard sensor characteristics, such as absolute error, signal to noise ratio, root mean square error, sensitivity, hysteresis, and measurement range.

All the following information about sensor characteristics is from [44].



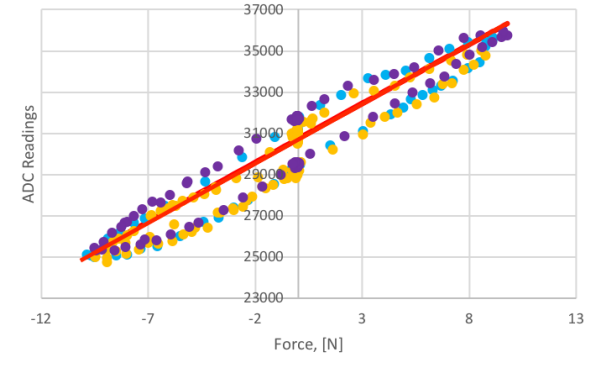
(a) X-direction



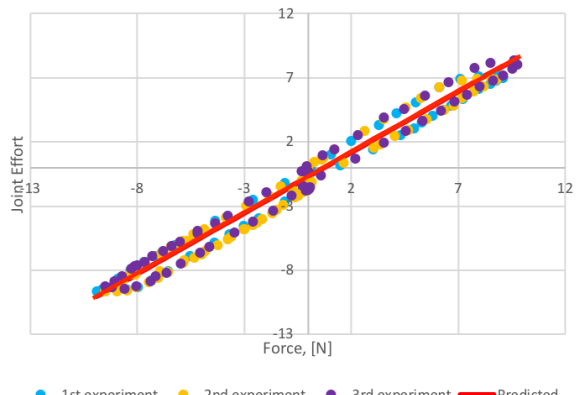
(b) Y-direction

Figure 3.23: Calibration Results of XY Device during Loading and Unloading ( $n=3$ )

The accuracy of the developed sensory systems was assessed using the Root Mean



(a) Z Device



(b) Joint Effort

Figure 3.24: Calibration Results in Z-direction during Loading and Unloading ( $n=3$ )

Square Error (RMSE), which is:

$$RMSE = \sqrt{\frac{\sum_{i=1}^n (\hat{y}_i - y_i)^2}{n}} \quad (3.15)$$

where  $\hat{y}_i$  is predicted with equation (3.6) force value ;  $y_i$  is observed "actual" force value found using load cell and Polaris;  $n$  is number of observations. RMSE values of all systems are high, meaning low accuracy of the developed system.

The error is the difference between the actual value of the force and the value produced by the system (Equation 3.16). Errors are related to accuracy and can be caused by different sources. In our case all errors were higher than 0.05 N, meaning that system does not meet accuracy requirements.

$$error = |\hat{y}_i - y_i| \quad (3.16)$$

One of the measurements of signal quality is signal-to-noise ratio (SNR). A higher value of SNR means the clear acquisitions with low signal distortions and artifacts caused by unwanted noise. It is defined as:

$$SNR = \frac{\mu}{\sigma} \quad (3.17)$$

where  $\mu$  is the mean value of the signal,  $\sigma$  is the standard deviation of the noise. SNR values for all systems are bigger than 1, meaning that all systems have relatively low noise.

The slope of the calibration curve is used for the sensitivity  $S$  calculation.

$$S = Dy/Dx \quad (3.18)$$

where  $Dy$  is the incremental change in the sensors output,  $Dx$  is the incremental change of the force. All the systems have relatively high sensitivity.

Resolution is the smallest change of the applied force that gives a noticeable change

in the sensor output, it is limited by the signal noise. Devices have higher resolution than required 0.3 N.

The linearity of the system is the proximity of the calibration curve to the straight line.  $R^2$  is used to evaluate linearity by measuring the closeness of the measured data to the fitted regression line. Generally, strain gauges have the linear response with deformation and all sensors showed high linearity with  $R^2$  higher than 90%.

Hysteresis is the difference between sensor outputs when the sensor is loaded versus unloaded. All sensors have shown hysteresis, up to 2.8 N. The Z-Device shows the highest hysteresis, the possible reason could be small thickness of the plate (where sensors are attached), that causes deformation during loading and unloading to follow different path. Another reason could be unevenness of the contact between the ball bearings and the rings. Hysteresis of the joint effort method can be explained by the complicated mechanical structure of the robot arm. Possible explanation of the X-Y Device hysteresis is uneven contact between the device and the instrument shaft. Meaning for all devices hysteresis can be caused by imperfections of mechanical structures.

The measurement range consists of the maximum and minimum values of the force that can be measured with created systems. For the created system, it corresponds to force values, when the output signal reaches saturation. However, for Z-directional measurements, when z-component of the applied force was higher than 12 N it caused sliding of the sterile adapter. Meaning physical limitation for Z-direction force mea-

surements. All designed devices measure forces in slightly higher than  $\pm 11N$  range.

When the applied force exceeds the specified range, the device readings can be used to trigger safety alert.

Precision represents the ability of the system to give the same output under the same conditions. The precision of the system was assessed by the standard deviation of the sensor outputs when similar forces were applied. All sensors have low precision, which is reflected in high absolute errors values.

All sensor characteristics were calculated for X-Y device, Z-device, and Z-direction evaluation joint effort method and provided in the Table 3.3. For each sensor, the calculated sensor characteristics are average values from the results of 3 trials.

Table 3.3: Sensors Characteristics

	X-sensor	Y-sensor	Z-sensor	Joint Effort
Error $\pm$ SD, N	$0.059 \pm 0.435$	$0.017 \pm 0.755$	$-0.716 \pm 1.324$	$-1.411 \pm 0.672$
RMSE	0.44	0.75	1.5	1.56
S/N	2888	3041	114	566
Noise SD, N	0.011	0.004	0.115	0.017
Sensitivity	911	1030	618	0.977
Precision, N	0.4	0.65	0.63	0.35
Resolution, N	0.03	0.02	0.2	0.03
$R^2$	0.965	0.924	0.938	0.963
Range, N	-19 to 23	-18 to 20	-12 to 12	-12 to 12
Hysteresis, N	0.99	2.4	2.8	1.2

### 3.7.2 Calibration Curve Dependence from Sterile Adapter Position

Movement of the sterile adapter joint, which is at the proximal end of the instrument, causes change of the moment arm length ( $L_{gauge}$  in Figure 3.25).

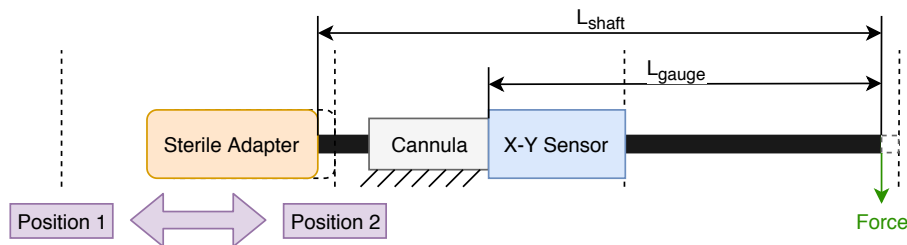


Figure 3.25: Sterile Adapter Movement

The force applied on the X-Y sensor  $F_{sensor}$  linearly depends on the moment arm length:

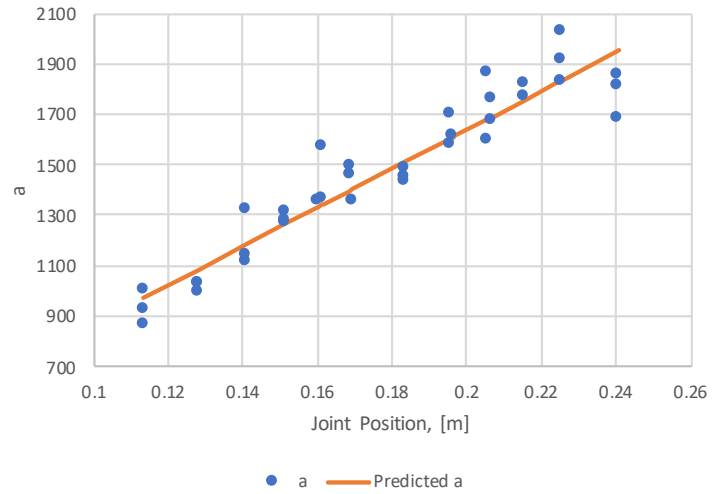
$$F_{sensor} = \frac{L_{shaft}}{L_{gauge}} \cdot F_{tool} \quad (3.19)$$

where  $F_{tool}$  is the force applied on the tool end,  $L_{shaft}$  is the length of the shaft.

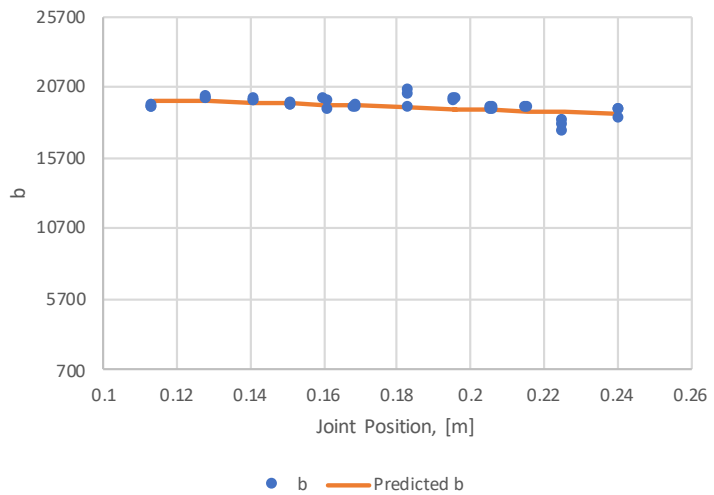
The dependence between position of the sterile adapter and calibration curve constants ( $a$  and  $b$  from equation 3.6) is linear for X and Y force components (Figures 3.26 - 3.27). We ran 3 trials for each position.

The  $R^2$  of constant  $a$  is 0.9 for X-component of the force, 0.827 for Y-component. The low linear fit is caused by considerable systematic errors of the sensors.

Constant  $b$  does not depend on the sterile adapter position and changes due to systematic errors and noise in the system.

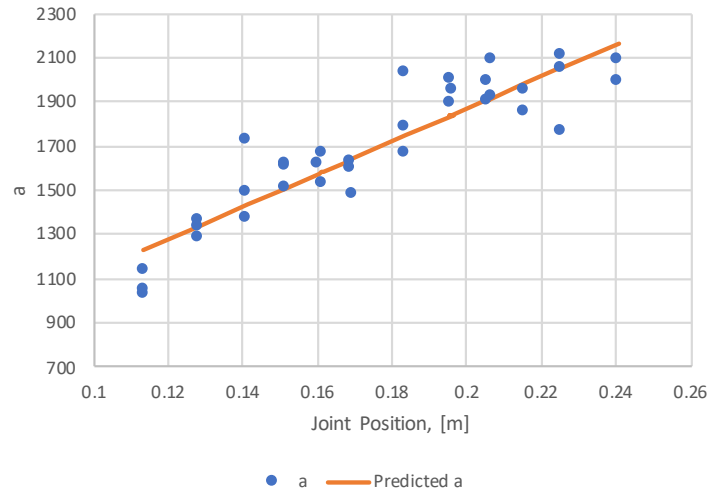


(a) Constant a

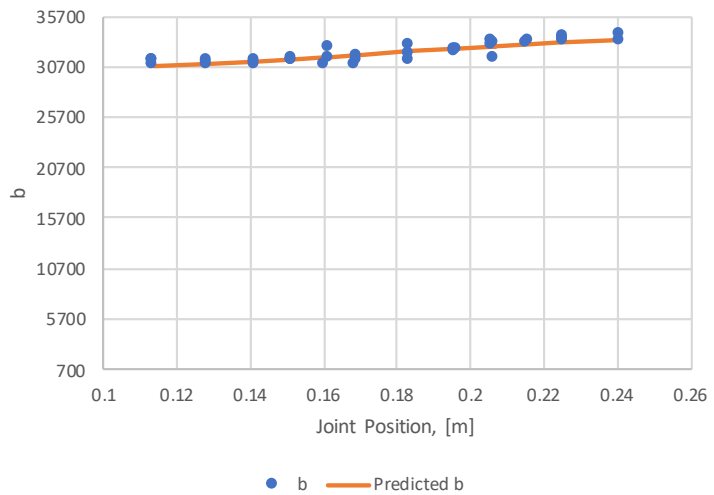


(b) Constant b

Figure 3.26: Sterile Adapter Position Calibration Results for X-direction



(a) Constant a



(b) Constant b

Figure 3.27: Sterile Adapter Position Calibration Results for Y-direction

# Chapter 4

## Discussion and Conclusion

The previous chapter discussed all aspects of the force sensor design for the daVinci robot, concluding with calibration results of the created sensors. The results have shown that the developed system is linear and has high sensitivity, appropriate measuring range, high resolution, and low noise. In addition, the results from FFT analysis have shown that the developed PCB gives low noise output. The noise is outside frequency range of the original signal and can be easily filtered out using digital low pass filter.

At the same time, the sensory system has high absolute errors, high RMSE, low precision, and significant hysteresis. Figure 4.1 shows X-component of the force measured at the same time using the X-Y device and using "actual force" data from the load cell. The error value changes simultaneously with rapid changes of the force applied. Taking into account, the low noisiness of the system, plausible explanation

of the fluctuations in the output signal is systematic errors. Important to note, that the errors could be related to the high hysteresis of the sensors.

## 4.1 Mechanical Design Issues

The force-sensing devices were designed so they can easily fit the daVinci cannula and the sterile adapter. The tolerances are compensated by adjustment of the set screws, giving good modularity of the system.

One of the disadvantages is the addition of the weight to the arm, that can alter robot performance. Taking into account, that the device will be placed close to the center of rotation of the robot arm, it will have minimal effect on the moment of inertia in comparison to sensors added to the grippers.

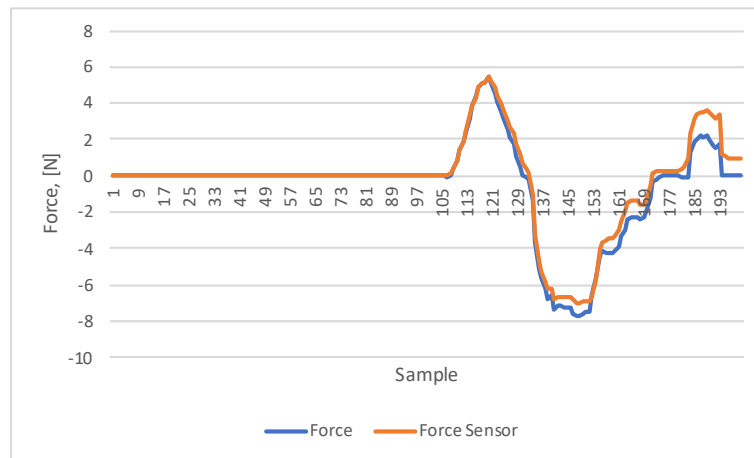


Figure 4.1: Actual and Measured Forces in X-direction

The calibration curve for Y-directional sensor has higher absolute error values, higher RMSE and lower linearity in comparison to X-directional sensor. The reason

for that could be mechanical design issues caused by manufacturing problems (Figure 4.2). Different thicknesses of the walls, where sensors applied, cause different strain values for positive and negative directions of the force.

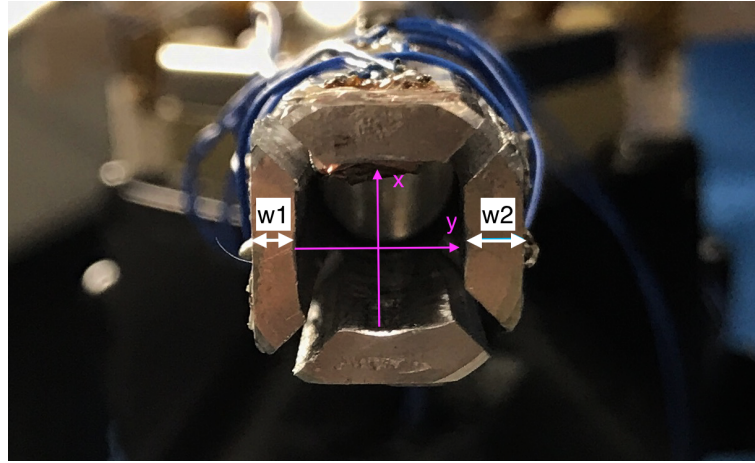


Figure 4.2: Lower Face of the X-Y Device without Tool Shaft

Comparison of two Z-component of the force measurement methods has shown, that Z Device has lower signal-to-noise ratio, lower resolution, lower linearity, and higher hysteresis. Even though the joint effort method is slightly better than the created device, it does not comply with all sensor requirements, and it is hard to change the output results for this method. The major advantage of the created Z Device is the ability to improve it. For example, hysteresis can be reduced by changing the force measurement plate material and its thickness.

The system has separate Wheatstone bridges for each direction, giving the ability to measure each component of the force independently. However, Z Device and the X-Y device cannot work together at the same time, because created X-Y device takes the Z-component of the force and slightly restricts rotation of the shaft. In order to

solve that issue, we can change the mechanical design of the X-Y device by increasing the size of the sleeve and adding slippery material between the shaft and the sleeve (Figure 4.3). However, it will cause other issues with increased incision size to 1.9 cm. It is still in the appropriate range (1-2 cm) [45], however, the patient recovery time would increase. Another option could be moving the X-Y device on the top of the cannula or changing the cannula design and applying sensors on it.

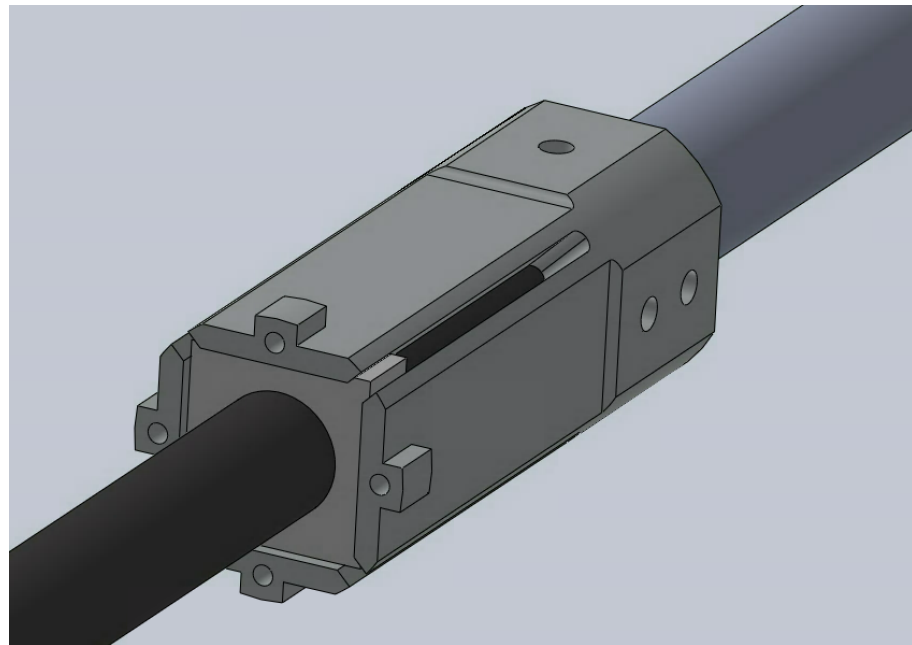


Figure 4.3: New X-Y Device Design

Both devices should undergo sterilization. XY device goes inside the patient, meaning that it should be created using biocompatible materials. The current version of the device is not biocompatible. The biocompatibility can be achieved using stainless steel as a device material and biocompatible epoxy to cover strain gauges, also Teflon coated wires should be used for all electrical connections. Use of stainless

steel will require the change of the device dimensions since the material has different elasticity.

## 4.2 Electrical Design Issues

The real-time haptic feedback requires minimum data acquisition speed to be 1 kHz [34]. However, the current maximum speed is 588 Hz due to the limitation of data transfer speed of serial communication (115.2 Kbps). In order to increase the speed, the communication channel can be changed to SPI (up to 10 Mbps) [46] or one of the wireless protocols, such as Bluetooth (up to 1 Mbps) or wifi (up to 100 Mbps) [47]. Also, the communication protocol between microcontroller and ADC can be changed from SPI (5.8 kHz) to the faster parallel communication. Additionally, the microcontroller can be changed to faster one, so it can support wireless communication. All these changes require the change of the PCB design and microcontroller software.

Bandwidth of the noise signal is in range 2.5 kHz and higher, meaning the need in low pass filter with cutoff frequency 2 kHz. It can be integrated in the system using digital or analog filtering.

Also, in the PCB the amount of Wheatstone bridges and ADCs should be increased from 2 to 4 to reduce the overall size of the system by removing second PCB and master-slave communication.

## 4.3 Conclusion

The created sensor gives 3-DOF force feedback by using lateral force sensing in a compact modular approach, a novel axial force sensing approach, and a custom ROS-enabled sensor interface. A new calibration approach of the force sensing devices was created. The contributions show that it is possible to add force-feedback in the daVinci robot without major changes of the existing system. However, not all of the requirements for the force measuring system were satisfied, meaning that the sensors need further improvements in both electrical and mechanical designs.

# References

- [1] Intuitive surgical, inc. - da vinci surgical system. [Online]. Available: <https://www.intuitivesurgical.com/>
- [2] A. M. Okamura, “Haptic feedback in robot-assisted minimally invasive surgery,” *Current opinion in urology*, vol. 19, no. 1, pp. 102–107, 2009.
- [3] C. R. Wagner, N. Stylopoulos, P. G. Jackson, and R. D. Howe, “The Benefit of Force Feedback in Surgery: Examination of Blunt Dissection,” *Presence: Teleoperators and Virtual Environments*, vol. 16, no. 3, pp. 252–262, May 2007.
- [4] M. Yiasemidou, D. Glassman, P. Vasas, S. Badiani, and B. Patel, “Faster simulated laparoscopic cholecystectomy with haptic feedback technology,” Oct. 2011. [Online]. Available: [https://www.dovepress.com/faster-simulated-laparoscopic-cholecystectomy-with-haptic-feedback-tec-peer-reviewed-article-](https://www.dovepress.com/faster-simulated-laparoscopic-cholecystectomy-with-haptic-feedback-tec-peer-reviewed-article)
- [5] M. E. Currie, A. Talasaz, R. Rayman, M. W. A. Chu, B. Kiaii, T. Peters, A. L. Trejos, and R. Patel, “The role of visual and direct force feedback in roboticsassisted mitral valve annuloplasty,” *The International Journal of Medical Robotics and Computer Assisted Surgery*, vol. 13, no. 3, Sep. 2017.
- [6] C. E. Reiley, T. Akinbiyi, D. Burschka, D. C. Chang, A. M. Okamura, and D. D. Yuh, “Effects of Visual Force Feedback on Robot-Assisted Surgical Task Performance,” *The Journal of thoracic and cardiovascular surgery*, vol. 135, no. 1, pp. 196–202, Jan. 2008.
- [7] O. A. J. v. d. Meijden and M. P. Schijven, “The value of haptic feedback in conventional and robot-assisted minimal invasive surgery and virtual reality training: a current review,” *Surgical Endoscopy*, vol. 23, no. 6, pp. 1180–1190, Jun. 2009.

- [8] M. Tavakoli, *Haptics for Teleoperated Surgical Robotic Systems*. World Scientific, 2008, google-Books-ID: 9UNkDQAAQBAJ.
- [9] R. H. Taylor and D. Stoianovici, “Medical robotics in computer-integrated surgery,” *IEEE Transactions on Robotics and Automation*, vol. 19, no. 5, pp. 765–781, Oct. 2003.
- [10] A. R. Lanfranco, A. E. Castellanos, J. P. Desai, and W. C. Meyers, “Robotic surgery,” *Annals of Surgery*, vol. 239, no. 1, pp. 14–21, 2004.
- [11] B. S. Peters, P. R. Armijo, C. Krause, S. A. Choudhury, and D. Oleynikov, “Review of emerging surgical robotic technology,” *Surgical Endoscopy*, vol. 32, no. 4, pp. 1636–1655, 2018.
- [12] Senhance surgical robotic system by TransEnterix. [Online]. Available: <https://www.transenterix.com/>
- [13] C. P. Delaney, A. C. Lynch, A. J. Senagore, and V. W. Fazio, “Comparison of robotically performed and traditional laparoscopic colorectal surgery,” *Diseases of the Colon & Rectum*, vol. 46, no. 12, pp. 1633–1639, Dec. 2003.
- [14] M. Morino, L. Pellegrino, C. Giaccone, C. Garrone, and F. Rebecchi, “Randomized clinical trial of robot-assisted versus laparoscopic Nissen fundoplication,” *British Journal of Surgery*, vol. 93, no. 5, pp. 553–558, May 2006.
- [15] I. E. Nakadi, C. Mlot, J. Closset, V. D. Moor, K. Btroune, P. Feron, P. Lingier, and M. Gelin, “Evaluation of da Vinci Nissen Fundoplication Clinical Results and Cost Minimization,” *World Journal of Surgery*, vol. 30, no. 6, pp. 1050–1054, Jun. 2006.
- [16] P. Kornprat, G. Werkartner, H. Cerwenka, H. Bacher, A. El-Shabrawi, P. Rehak, and H. J. Mischinger, “Prospective study comparing standard and robotically assisted laparoscopic cholecystectomy,” *Langenbeck’s Archives of Surgery*, vol. 391, no. 3, pp. 216–221, Jun. 2006.
- [17] B. T. Bethea, A. M. Okamura, M. Kitagawa, T. P. Fitton, S. M. Cattaneo, V. L. Gott, W. A. Baumgartner, and D. D. Yuh, “Application of Haptic Feedback to

Robotic Surgery,” *Journal of Laparoendoscopic & Advanced Surgical Techniques*, vol. 14, no. 3, pp. 191–195, Jun. 2004.

- [18] L. Meli, C. Pacchierotti, and D. Prattichizzo, “Sensory subtraction via cutaneous feedback in robot-assisted surgery,” *Mechanisms and Machine Science*, vol. 38, pp. 121–130, 2016.
- [19] M. B. Hong and Y. H. Jo, “Design and evaluation of 2-DOF compliant forceps with force-sensing capability for minimally invasive robot surgery,” *IEEE Transactions on Robotics*, vol. 28, no. 4, pp. 932–941, 2012.
- [20] C. Ho, E. Tsakonas, K. Tran, K. Cimon, M. Severn, M. Mierzwiński-Urban, J. Corcos, and S. Pautler, *HEALTH SERVICES IMPACT*. Canadian Agency for Drugs and Technologies in Health, 2011. [Online]. Available: <https://www.ncbi.nlm.nih.gov/books/NBK168924/>
- [21] H. Su, I. I. Iordachita, J. Tokuda, N. Hata, X. Liu, R. Seifabadi, S. Xu, B. Wood, and G. S. Fischer, “Fiber-optic force sensors for MRI-guided interventions and rehabilitation: A review,” *IEEE Sensors Journal*, vol. 17, no. 7, pp. 1952–1963, 2017.
- [22] J. Peirs, J. Clijnen, D. Reynaerts, H. V. Brussel, P. Herijgers, B. Corteville, and S. Boone, “A micro optical force sensor for force feedback during minimally invasive robotic surgery,” *Sensors and Actuators A: Physical*, vol. 115, no. 2, pp. 447 – 455, 2004, the 17th European Conference on Solid-State Transducers.
- [23] W. Schwalb, B. Shirinzadeh, and J. Smith, “A forcesensing surgical tool with a proximally located force/torque sensor,” *The International Journal of Medical Robotics and Computer Assisted Surgery*, vol. 13, no. 1, p. e1737, 2017.
- [24] A. I. Aviles, S. M. Alsaleh, J. K. Hahn, and A. Casals, “Towards retrieving force feedback in robotic-assisted surgery: A supervised neuro-recurrent-vision approach,” *IEEE Transactions on Haptics*, vol. 10, no. 3, pp. 431–443, 2017.
- [25] Sang Hongqiang, Yun Jintian, Monfaredi Reza, Wilson Emmanuel, Fooladi Hadi, and Cleary Kevin, “External force estimation and implementation in robotically assisted minimally invasive surgery,” *The International Journal of Medical Robotics and Computer Assisted Surgery*, vol. 13, no. 2, p. e1824, 2017.

- [26] S. M. Yoon, W. J. Kim, and M. C. Lee, “Design of bilateral control for force feedback in surgical robot,” *International Journal of Control, Automation and Systems*, vol. 13, no. 4, pp. 916–925, 2015.
- [27] HBM. (2017) Piezoelectric or Strain Gauge Based Force Transducers? [Online]. Available: <https://www.hbm.com/en/3719/piezoelectric-or-strain-gauge-based-force-transducers/>
- [28] A. sensors. (2017) Piezoelectric Sensors and Strain Gauge-based Force Transducers: Principles in Force Measurement. [Online]. Available: <http://www.azosensors.com/article.aspx?ArticleID=281>
- [29] N. I. L. Azaman, M. A. Ayub, and A. A. Ahmad, “Characteristic and sensitivity of quantum tunneling composite (QTC) material for tactile device applications,” in *2016 7th IEEE Control and System Graduate Research Colloquium (ICSGRC)*, 2016, pp. 7–11.
- [30] “Quantum tunnelling composites: Characterisation and modelling to promote their applications as sensors,” *Sensors and Actuators A: Physical*, vol. 164, no. 1, pp. 46–57, 2011.
- [31] D. C. W. Friedman, T. S. Lendvay, and B. Hannaford, “Instrument failures for the da vinci surgical system: a food and drug administration MAUDE database study,” *Surgical Endoscopy*, vol. 27, no. 5, pp. 1503–1508, 2013.
- [32] S. K. Prasad, M. Kitagawa, G. S. Fischer, J. Zand, M. A. Talamini, R. H. Taylor, and A. M. Okamura, “A modular 2-DOF force-sensing instrument for laparoscopic surgery,” in *Medical Image Computing and Computer-Assisted Intervention - MICCAI 2003*, ser. Lecture Notes in Computer Science. Springer, Berlin, Heidelberg, 2003, pp. 279–286. [Online]. Available: [https://link.springer.com/chapter/10.1007/978-3-540-39899-8\\_35](https://link.springer.com/chapter/10.1007/978-3-540-39899-8_35)
- [33] I. Mack, S. Ferguson, K. Rafferty, S. Potts, and A. Dick, “Interactive force-sensing feedback system for remote robotic laparoscopic surgery,” *Transactions of the Institute of Measurement and Control*, vol. 34, no. 4, pp. 376–387, 2012.

- [34] Seungmoon Choi and H. Tan, “Effect of update rate on perceived instability of virtual haptic texture,” vol. 4. IEEE, 2004, pp. 3577–3582. [Online]. Available: <http://ieeexplore.ieee.org/document/1389970/>
- [35] ROS.org | is ROS for me? [Online]. Available: <http://www.ros.org/is-ros-for-me/>
- [36] ASM material data sheet. [Online]. Available: <http://asm.matweb.com/search/SpecificMaterial.asp?bassnum=ma6061t6>
- [37] MICRO-MEASUREMENTS. (2014) Surface Preparation for Strain Gage Bonding. [Online]. Available: <http://www.vishaypg.com/docs/11129/11129B129.pdf>
- [38] V. P. Group. Cea Strain Gage Installation with M-Bond 200 Adhesive (Training Video) - Micro-Measurements. Youtube. [Online]. Available: <https://www.youtube.com/watch?v=SjXpF61HRys>
- [39] Printed circuit board manufacturer & PCB assembly | advanced circuits. [Online]. Available: <http://www.4pcb.com/>
- [40] F. J. Harris, “On the use of windows for harmonic analysis with the discrete fourier transform,” *Proceedings of the IEEE*, vol. 66, no. 1, pp. 51–83, 1978.
- [41] Filtering and smoothing data - MATLAB & simulink. [Online]. Available: <https://www.mathworks.com/help/curvefit/smoothing-data.html>
- [42] Introduction to arduino SPI library with LTC1286 and DAC714. [Online]. Available: <https://www.allaboutcircuits.com/projects/arduino-spi-library-ltc1286-dac714/>
- [43] “LTC1864/LTC1865 - power, 16-bit, 250ksps 1- and 2-channel ADCs in MSOP,” p. 24.
- [44] K. Kalantar-zadeh, *Sensors Characteristics*. Springer US, 2013, pp. 11–28. [Online]. Available: [http://link.springer.com/10.1007/978-1-4614-5052-8\\_2](http://link.springer.com/10.1007/978-1-4614-5052-8_2)
- [45] Laparoscopy and laparoscopic surgery. surgery information. [Online]. Available: <https://patient.info/health/laparoscopy-and-laparoscopic-surgery>

- [46] UART vs SPI vs i2c | difference between UART,SPI and i2c. [Online]. Available: <http://www.rfwireless-world.com/Terminology/UART-vs-SPI-vs-I2C.html>
- [47] Wireless protocols - WiFi, bluetooth, BT, BTLE, GPS, GPRS, 6lowpan, zigbee, RoweBots bluetooth stack - RoweBots. [Online]. Available: <http://rowebots.com/en/products/unison-rtos-article/wireless-protocols>

# Appendix A

## Appendix A. Circuit

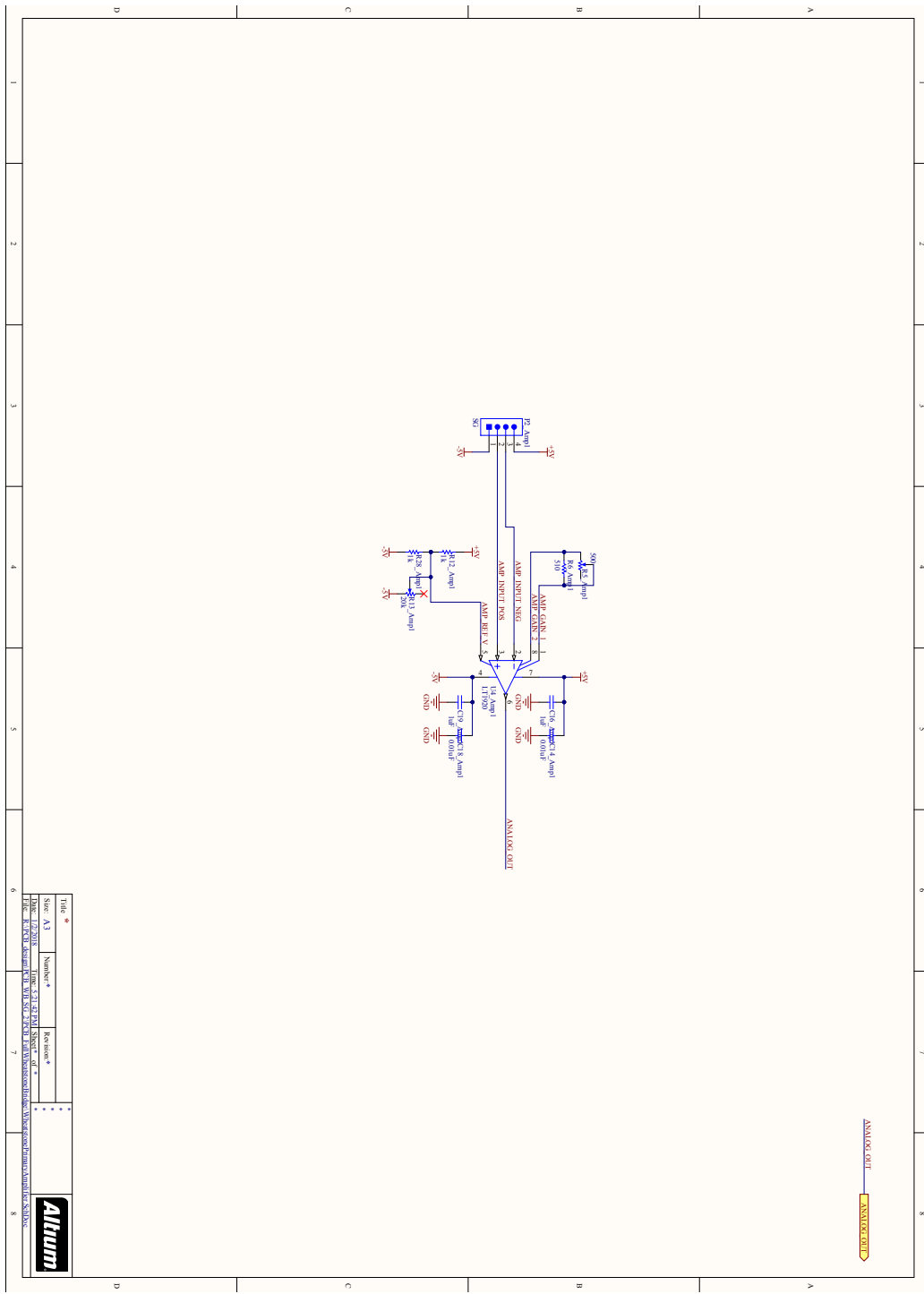


Figure 4.4: 1st Instrumentation Amplifier

## Appendix A. Circuit

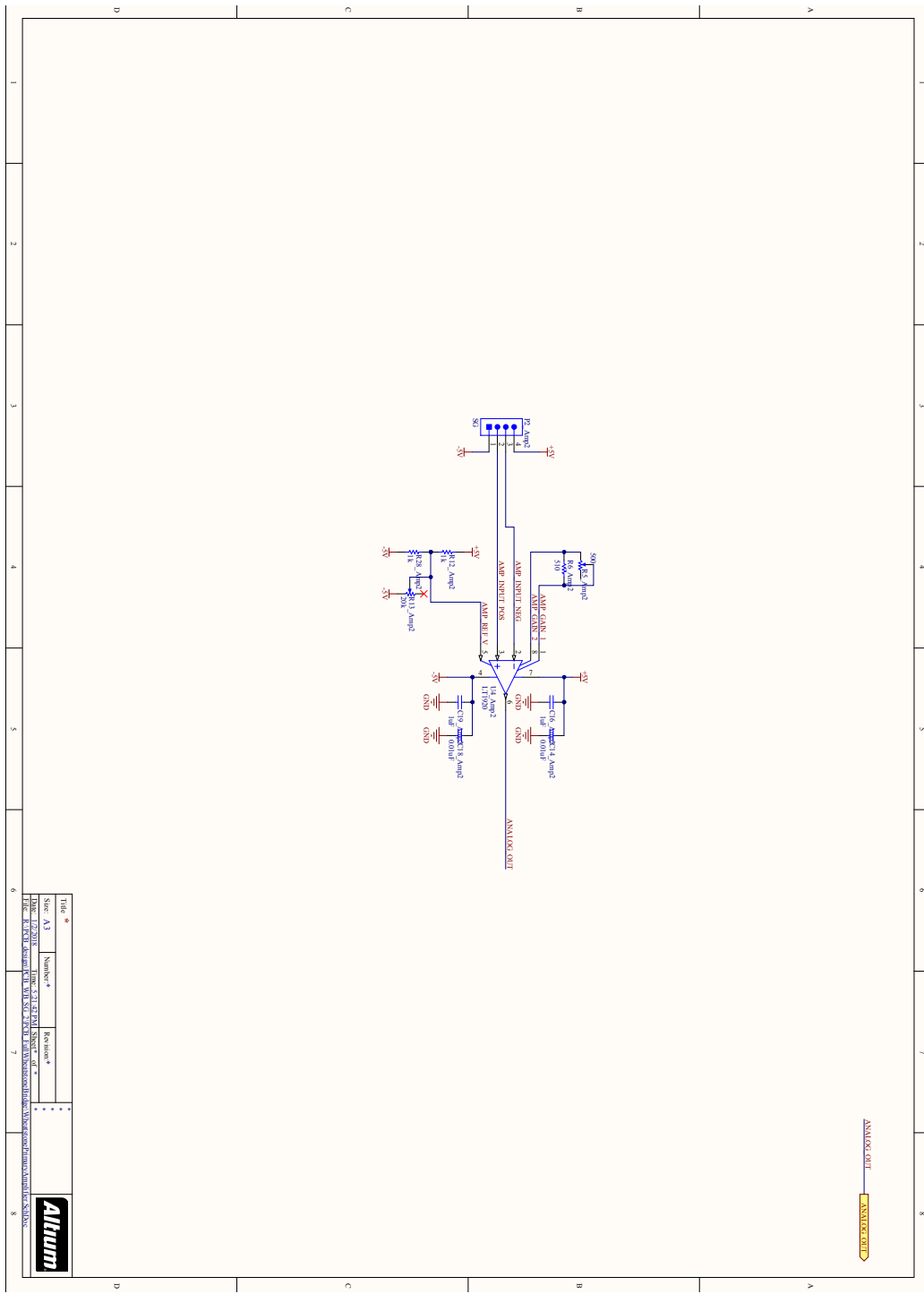


Figure 4.5: 2nd Instrumentation Amplifier

Appendix A. *Circuit*

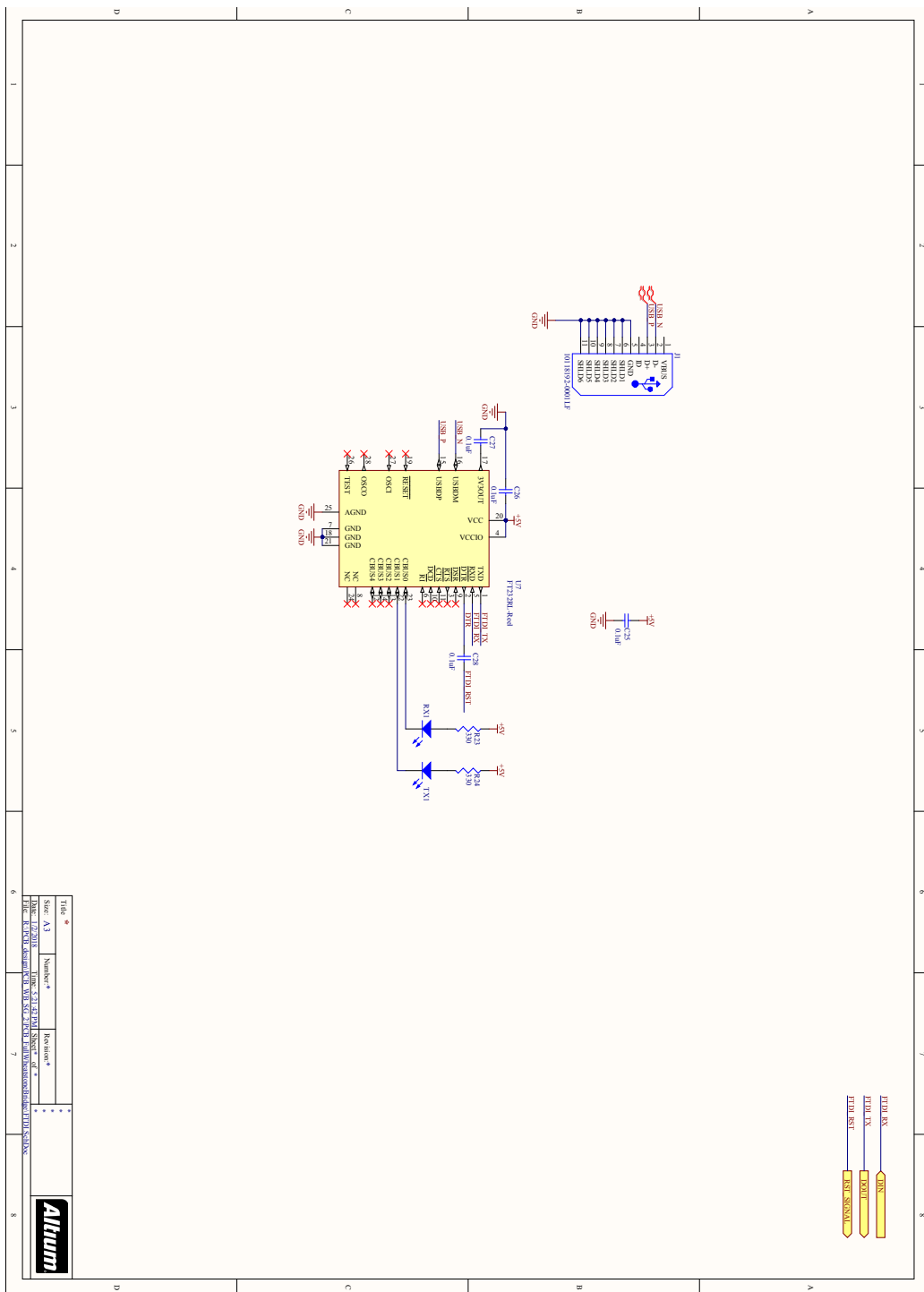


Figure 4.6: USB-UART Interface

## Appendix A. *Circuit*

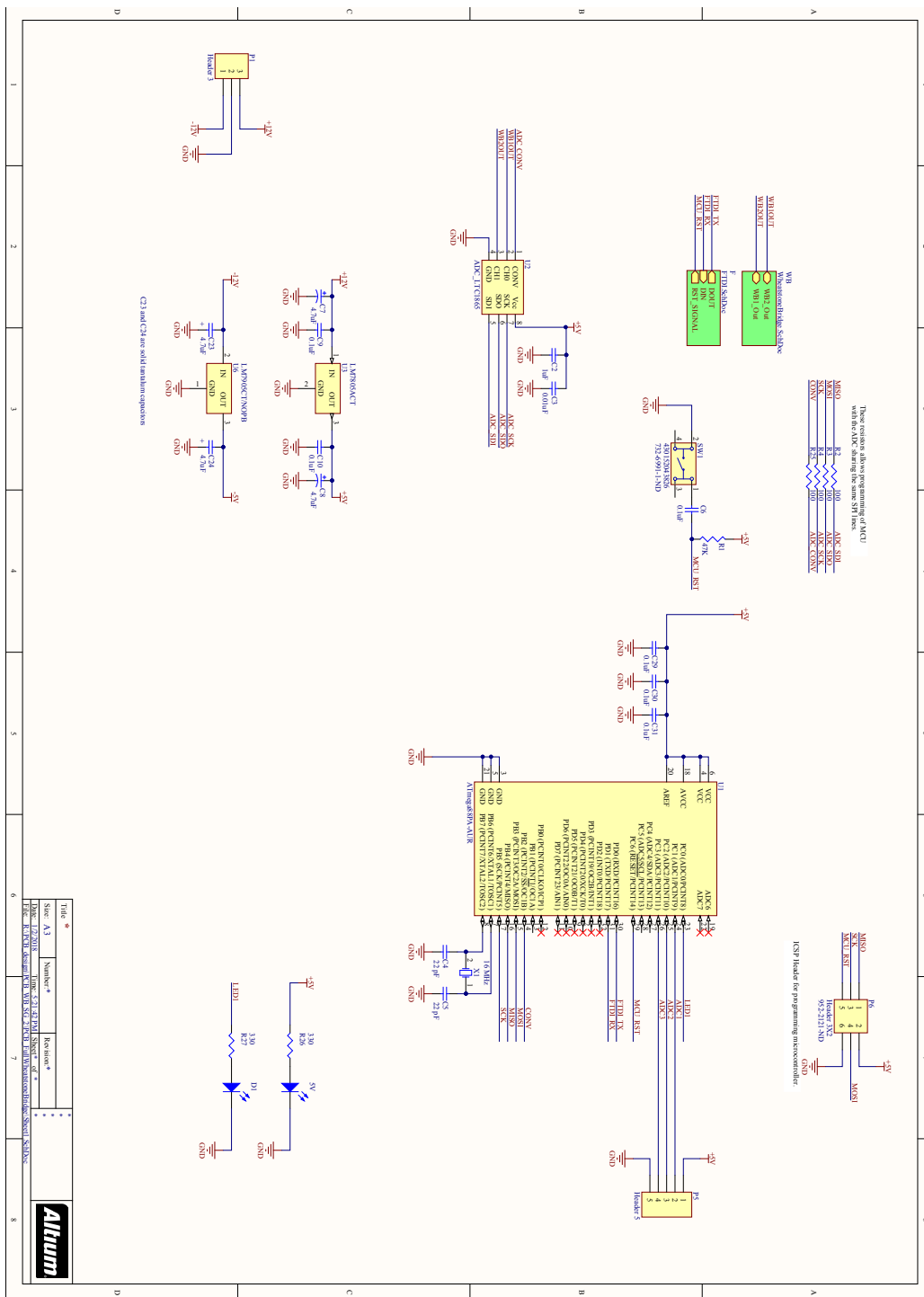


Figure 4.7: Microcontroller and Power Source

## Appendix A. Circuit

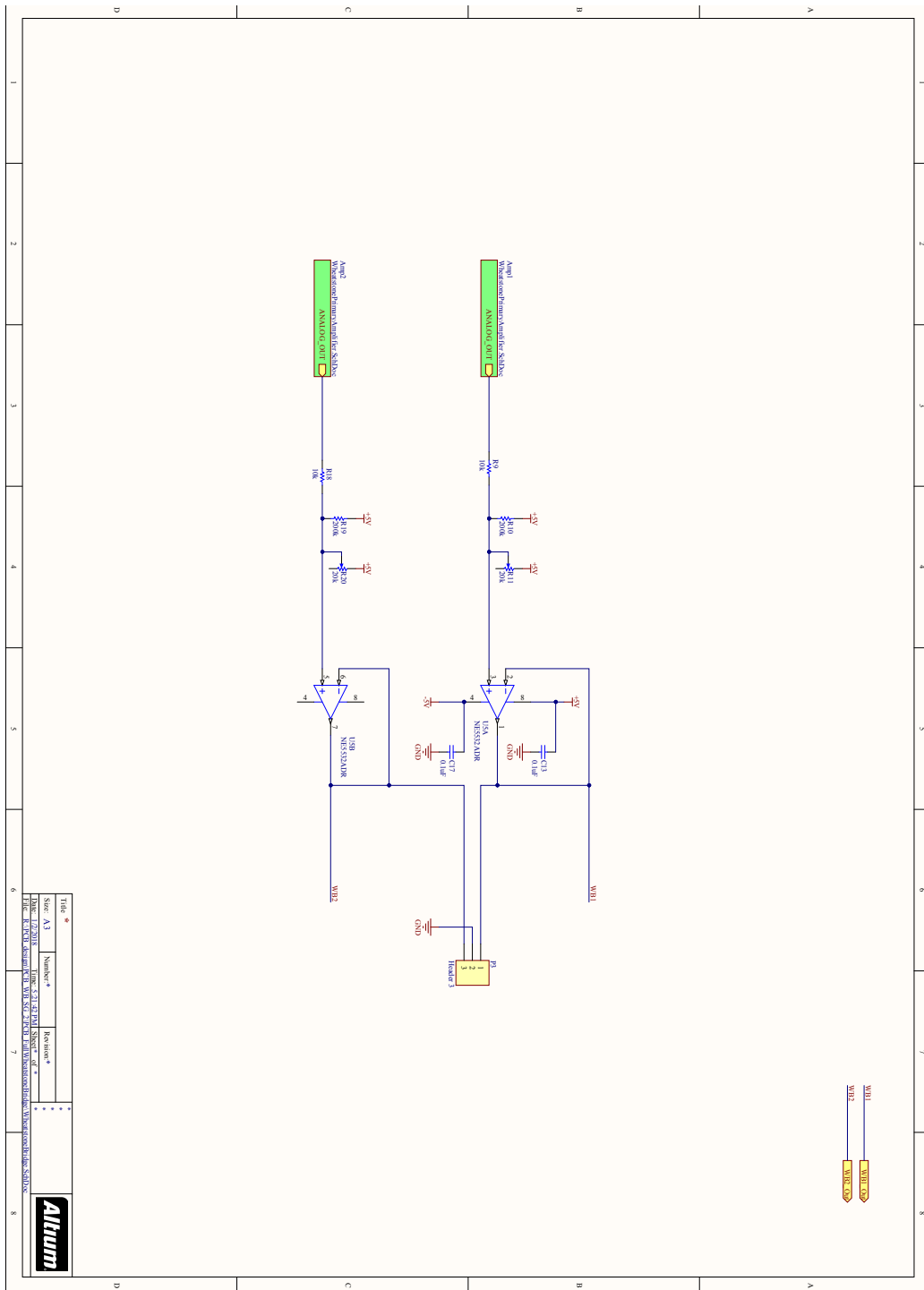


Figure 4.8: Voltage Converter

## Appendix A. *Circuit*

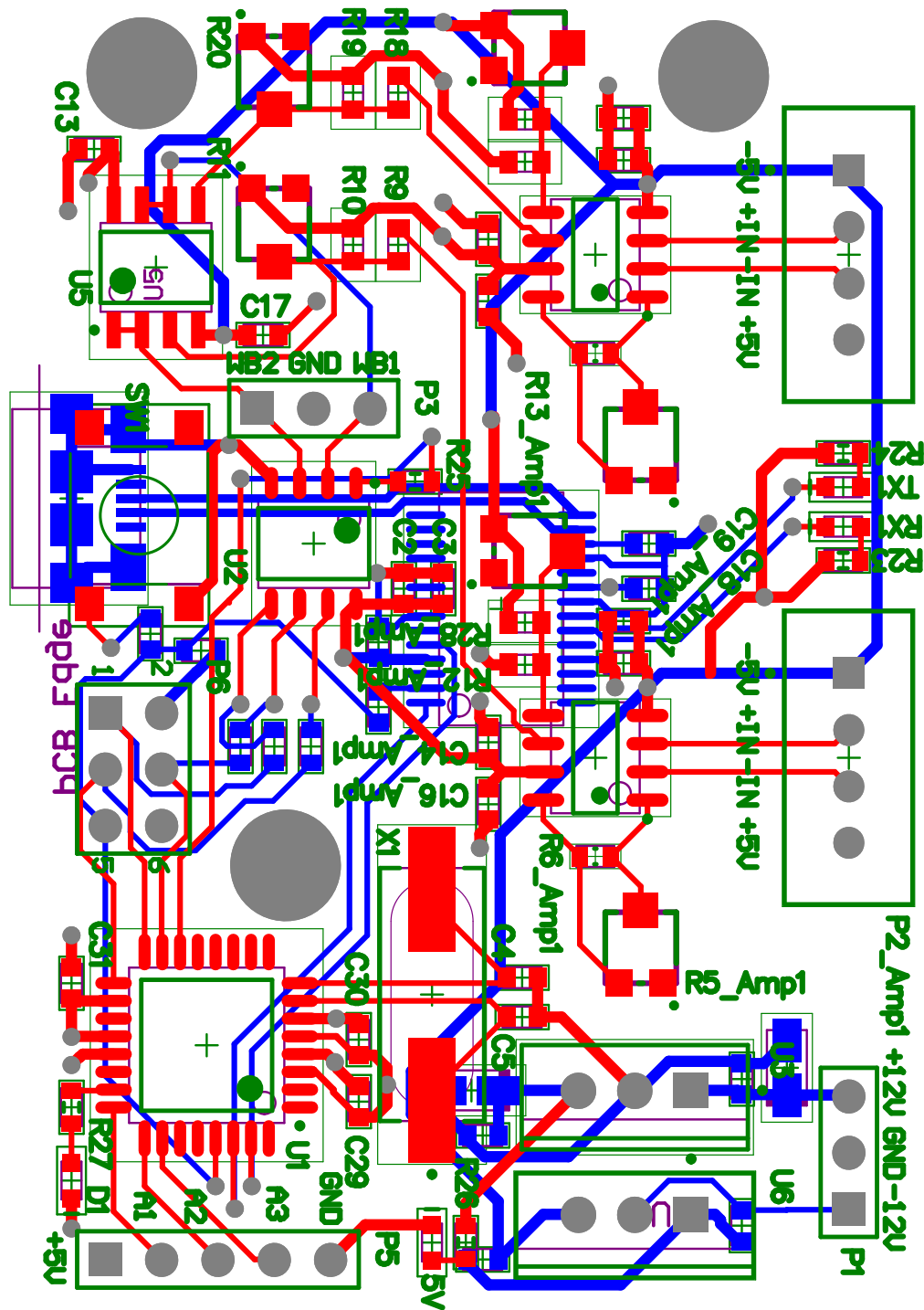


Figure 4.9: PCB Layout

## Appendix B

## Appendix B. Bill of Materials

Comment	Description	Designator	Footprint	Quantity	Unit Price	Total Price
<b>PCB Materials</b>						
<b>Capacitors</b>						
	1uF	C2, C16_Apm1, C19_Ampl, C16_Amp2, C19_Amp2	0603	5	0.05\$	0.23\$
	0.1uF	C13, C17, C27, C26, C28, C25, C9, C10, C6, C29, C30, C31	0603	12	0.08\$	0.91\$
	22pF	C4, C5	0603	2	0.10\$	0.20\$
	0.01uF	C3, C14_Amp1, C18_Ampl, C14_Amp2, C18_Amp2	0603	5	0.08\$	0.38\$
	CAP TANT 4.7UF 16V 20% 0603	C23, C24	0603	2	0.55\$	1.09\$
	Standard Tantalum, 4.7 uF, +/- 10%, 16 V, -55 to 125 degC, 2-Pin SMD (1206), RoHS, Tape and Reel	C7, C8	1206	2	0.24\$	0.48\$
<b>Resistors</b>						
100	100R 0.1W 5% 0603 (1608 Metric) SMD	R2,R3,R4,R25	0603	4	0.30\$	1.20\$
330	330R 0.1W 5% 0603 (1608 Metric) SMD	R23,R24,R26,R27	0603	4	0.01\$	0.04\$
510	510R 0.1W 5% 0603 (1608 Metric) SMD	R6_Amp1, R6_Amp2	0603	2	0.09\$	0.17\$
1k	Chip Resistor, 1 KOhm, +/-1%, 0.1 W, -55 to 155 degC, 0603 (1608 Metric), RoHS, Tape and Reel	R12_Amp1, R12_Amp2, R28_Amp1, R28_Amp2	0603	4	0.30\$	1.20\$
47k	Chip Resistor, 47 KOhm, +/-1%, 0.1 W, -55 to 155 degC, 0603 (1608 Metric), RoHS, Tape and Reel	R1	0603	1	0.11\$	0.11\$
10k	Chip Resistor, 10 KOhm, +/-1%, 0.1 W, -55 to 155 degC, 0603 (1608 Metric), RoHS, Tape and Reel	R9, R18	0603	2	0.10\$	0.20\$
200K	Chip Resistor, 200 KOhm, +/-1%, 0.1 W, -55 to 155 degC, 0603 (1608 Metric), RoHS, Tape and Reel	R10, R19	0603	2	0.10\$	0.20\$
500	Trimpot	R5_Amp1, R5_Amp2	Trimpot_Cut_tape_3.4x3.4x2	2	1.28\$	2.55\$
20k	Trimpot	R11, R13_Amp1, R13_Amp2, R20	Trimpot_Cut_tape_3.4x3.4x2	4	1.28\$	5.11\$
<b>Other components</b>						
Switch 430152043826	WS-TASV SMD Tact Switch 6X6 mm	SW1	430152043826	1	0.47\$	0.47\$
ATmega328P	8-bit AVR Microcontroller, 8KB Flash, 512 Bytes EEPROM, 1KB SRAM, 32-pin TQFP, Industrial Grade (-40°C to 85°C), Reel	U1		1	2.20\$	2.20\$

Figure 4.10: PCB Materials Bill (1)

## Appendix B. Bill of Materials

ADC LTC1865		U2	LTC1865_SOIC8	1	13.20\$	13.20\$
Vol Reg LM7805ACT	Positive Voltage Regulator, 5 V, 1 A, 0 to 125 degC, 3-Pin TO-220, RoHS, Tube	U3	FAIR-TO-220-3	1	0.90\$	0.90\$
Instr Amp LT1920	Single Channel, Resistor Gain Programmable, Precision Instrumentation Operational Amplifier, 0.8 MHz Typical GBW, 1.2 V/us Typical SR, 4.6 to 40 V, 8-Pin SOIC (S8-8), Commercial, Pb-Free	U4_Amp1, U4_Amp2	LT-S8-8_L	2	6.28\$	12.56\$
Op Amp NE5532ADR	Dual Low-Noise Operational Amplifier, 10 to 30 V, 0 to 70 degC, 8-pin SOIC (D8), Green (RoHS & no Sb/Br)	U5	D0008A_M	1		0.00\$
Vol Reg LM7905CT/NOPB	3-Terminal Negative Regulator, 3-pin TO-220, Pb-Free	U6	NDE0003A	1	1.63\$	1.63\$
USB-UART FT232RL-Reel	USB UART Asynchronous Serial Data Transfer Chip, 28-pin SSOP, Tape and Reel	U7	SSOP-28_L	1	4.50\$	4.50\$
Crystal ABLS2-16.000 MHZ-D4Y-T	Low Profile Surface Mount Microprocessor Crystal, 16.000 MHz +/- 30 ppm, 180 Ohm, -40 to 85 degC, 2-Pin 11.4 x 4.7 x 3.3 mm SMD, RoHS, Tape and Reel	X1	ABRA-ABLS2-2_V	1	0.46\$	0.46\$
Micro USB 10118192-0001LF	Micro USB B Type Receptacle, -55 to 85 degC, 5-Pin SMD, RoHS, Tape and Reel	J1	FCI-10118192-0001LF-5_V	1	0.46\$	0.46\$
Header 3	Header, 3-Pin	P1, P3	HDR1X3	2	0.13\$	0.26\$
SG header	Male Header, Pitch 2.54 mm, 1 x 4 Position, Height 14.199 mm, Tail Length 3.302 mm, -55 to 105 degC, RoHS, Rail/Tube	P2_Amp1, P2_Amp2	TECO-5-103414-2_V	2	1.57\$	3.14\$
Header 5	Header, 5-Pin	P5	HDR1X5	1	0.25\$	0.25\$
Header 3X2	Header, 3-Pin, Dual row	P6	HDR2X3	1	0.24\$	0.24\$
Pwr supply	7.5V 7.5W AC/DC External Wall Mount Adapter Fixed Blade Input		237-2215-ND	2	10.52\$	21.04\$
LED 150060RS75000	SMD mono-color Chip LED, WL-SMCW, Red	5V, D1, RX1, TX1	0603_A	4	0.14\$	0.56\$
PCB	Manufactured at Advanced Circuits			1	66\$	66\$
					Total	141.95\$

Figure 4.11: PCB Materials Bill (2)

## Appendix B. Bill of Materials

Comment	Description	Quantity	Unit Price	Total Price
<b>Strain gauges and application materials</b>				
M-Bond 200 Adhesive		1	88.44\$	88.44\$
MCA-1, M-Prep Conditioner A,	2 oz (60 ml) bottle	1	19.36\$	19.36\$
MN5A-1, M-Prep Neutralizer 5A	2 oz (60 ml) bottle	1	19.36\$	19.36\$
GSP-1, gauze sponges, 1 package	3 in x 3 in	1	5.79\$	5.79\$
Solvent Degreaser CSM-2		1	20.00\$	20.00\$
M-Bond 200 Catalyst-C		1	13.71\$	13.71\$
Polyurethane		1	11.98\$	11.98\$
Isopropyl 70% Alcohol		1	2.00\$	2.00\$
Glass	150x150 mm	1	0.00\$	0.00\$
Tape		1	1.00\$	1.00\$
Strain gauges with pads 9SIA67055T3138	SODIAL 5 x BF350-3AA 3500 High-Precision Resistive Pressure Resistance Steel Strain Gauge (5 in package)	12	1.06\$	12.72\$
<b>Mechanical Design</b>				
Ball Bearings 6655K17	Thrust Ball Bearing for 1/2" Shaft Diameter, 15/16" OD, 0.249" Thick	2	2.80\$	5.60\$
Aluminum Rod 1610T13	6061 Aluminum, 11/2" Diameter, 1/2 Feet Long	1	2.57\$	2.57\$
Aluminum Rod 8974K11	6061 Aluminum, 3/4" Diameter, 1/2 Feet Long	1	3.17\$	3.17\$
Set Screws 92949A050	18-8 Stainless Steel Button Head Hex Drive Screw, 0-80 Thread Size, 1/8" Long, Packs of 100	1	5.19\$	5.19\$
Spring 9654K411	Steel Extension Spring with Loop Ends, Music-Wire, 2.5" Long, 0.188" OD, 0.025" Wire, Packs of 12	1	8.88\$	8.88\$
			<b>Total</b>	<b>219.77\$</b>

Figure 4.12: Mechanical and Strain Gauge Materials Bill